HIGH ALTITUDE OBSERVATORY
of
Harvard University and University of Colorado

TECHNICAL REPORT

Emission in the Hydrogen Balmer Lines and Continuum in the Flash Spectrum of the 1952 Total Solar Eclipse at Khartoum, Sudan

by

Russell Grant Athay

13 July 1953

ONR Contract Nonr-393(01)
Project NRL Req. 173 6-4-53 53

FOREWORD

A part of the research work on Contract Nonr 393(01) has been conducted by a graduate student, Mr. Russell Grant Athay, working under a cooperative research program in solar physics between High Altitude Observatory and the University of Utah. The Ph.D. thesis summarizing his work has been jointly supervised by the astrophysics group of the University of Utah and the research staff of the High Altitude Observatory. The thesis contains major results of the eclipse expedition conducted under the contract, and is therefore being issued herewith as a contract technical report.

The principal scientific results in this thesis will later be made the subject of published articles in the scientific literature. Such published articles will be distributed as additional technical reports under this contract.

Walter Orr Roberts, Director
High Altitude Observatory

13 July 1953

TABLE OF CONTENTS

	ABSTRACT	iii
I.	INTRODUCTION	1
II.	OBSERVATIONS AT THE ECLIPSE	3
III.	PHOTOMETRIC METHODS	
	A. Summary of Planned Photometric Program	11
	B. Photometric Program as Executed	13
	C. Method of Determining Characteristic Curves by Standard Lamp and Collimator	14
	D. Method of Determining Characteristic Curves by Use of the Coronal Continuum and the Data Panel Wedge	24
IV.	TABULATION OF INTENSITIES	38
V.	COMPARISON OF INTENSITIES WITH PREVIOUS OBSERVATIONS	53
VI.	PRELIMINARY INTERPRETATION OF DATA	59
	A. Preliminary Analysis of Balmer Continuum Data	63
	B. Hydrostatic Equilibrium	71
	C. Balmer Line Emission	75
	1. Self-absorption	78
	2. b_n Gradients	82
	3. Combined Effects of Self-absorption and b_n's	90
VII.	ACKNOWLEDGMENTS	95
VIII.	APPENDIX	97

ABSTRACT

Analysis of ultraviolet spectrograms of the chromospheric flash obtained at the 1952 solar eclipse at Khartoum, Sudan, presented serious photometric problems. Standardising exposures in the ultraviolet made at Khartoum were not successful because of a post-eclipse failure of the film advance mechanism. Characteristic curves obtained from standard lamp exposures made in Boulder after completion of the expedition could not be trusted to represent the photometric properties of the eclipse films, and were principally useful as a first approximation to the curves representing the eclipse spectrograms. In addition, there were uncertainties in the duration of the exposures on all except six spectrograms.

Methods were developed that allowed, in spite of these problems, entirely reliable determinations of the characteristic curves of the films made during the eclipse. A thorough, independent check on the consistency and accuracy of the final curves was possible and its result was entirely satisfactory.

The image of the coronal continuum extending beyond the moon's limb at right angles to the line of contacts was used to determine the relative exposures. Change with wavelength of film sensitivity, atmospheric absorption, and reflectivity of the mirror surfaces were evaluated and included as corrections to the photometry.

The densities of the hydrogen Balmer lines from H_8 to H_{31} and at four wavelengths in the Balmer continuum were measured at two points on the limb on 17 spectrograms at second contact. The microdensitometer at the McMath-Hulbert Observatory was used for the tracings. These densities were then

converted to give, after application of the photometric procedures, tables of corrected line intensities for 24 lines of the Balmer series at heights separated by 108 kms in the lower chromosphere, ranging from 100 kms to 3800 kms in height, as shown in Table 2, pages 48 and 49.

The values of line and continuum intensities were found to be internally consistent and it was demonstrated that systematic errors were negligibly small. The random errors were relatively small for photographic photometry.

The Balmer decrements agreed well with those obtained by Cillié and Menzel at the 1932 eclipse at the heights of the chromosphere where the observations overlap. However, the emission-height gradients of hydrogen are about 40% larger than in 1932, and the absolute intensities of the hydrogen emission at the base of the chromosphere were about five times as large as in 1932.

The emission-height curves were found to be well represented by

$$E_n = E_{n,o}\, e^{-\beta_n h}$$

except for lines H_8 to H_{11} below 2000 km. The values of β_n increased systematically from $\beta_8 = 1.4 \times 10^{8}\,cm^{-1}$ to $\beta_{31} = 2.1 \times 10^{-8}\,cm^{-1}$.

Preliminary interpretation of the observations revealed that the effects of self-absorption were pronounced, and also demonstrated that there were large departures from thermodynamic equilibrium in the sense that the b_n's were greater than one at 700 km and increased with height.

Preliminary analysis of the Balmer continuum data showed that the electron temperature was less than 12,000° K at chromospheric heights below 1000 km and that the temperature increased upward. The electron densities in the low chromosphere were found to be of the order of 10^{11} per cm^3.

A detailed determination of the thermodynamic structure of the solar chromosphere will be attempted by Dr. R. N. Thomas and his associates from the tabulated intensities given in this thesis, and will be the subject of later reports from the High Altitude Observatory.

I. INTRODUCTION

Spectrographic observations of the flash spectrum at the total solar eclipse in Khartoum, Sudan, on February 25, 1952 were made by the High Altitude Observatory of Harvard University and the University of Colorado. This work was supported by the Office of Naval Research and carried out in cooperation with the Naval Research Laboratory. A primary purpose of the expedition was to obtain observations of the solar chromosphere simultaneously in the optical-photographic and short-wave radio regions of the spectrum. These two sets of observations are to be used, in turn, as independent means of deducing the thermodynamic structure of the chromosphere.

The results of previous radio noise observations[1] gave electron temperatures of the order of 5000° K in the lower chromospheric layers. Temperatures of this same order were found by Cillié and Menzel[2] from the distribution of intensities in the Balmer continuum observed at the 1932 eclipse, and similar results were obtained by Goldberg[3] from the relative population of excited levels in Helium. On the other hand, line profile measurements by Redman[4] at the 1940 eclipse gave temperatures of the order of 30,000° K. Giovanelli[5] and others have pointed out that temperatures of this latter order are required to support the observed density gradients if one assumes a highly ionized atmosphere in hydrostatic equilibrium. In a series of papers, Thomas[6] showed further evidence in favor of a high temperature chromosphere.

At the present time there is considerable doubt about the actual thermodynamic conditions in the chromosphere. Not only are the observations

apparently conflicting, but theoreticians are also in disagreement as to the causes of the discrepancies. We hope that the present observations will help to resolve the apparent differences between the optical and radio noise observations by giving us an improved determination of the thermodynamic conditions in the chromosphere. The methods of analysis and the requirements for the optical observations were developed by Thomas.[7] The spectrographic equipment was designed by the High Altitude Observatory explicitly to fit these requirements, and to give the necessary data for this analytical method, namely, detailed spectrophotometric observations of the emission in the hydrogen Balmer and Paschen series.

Completion of the overall problem divides itself logically into two parts: (1) measurement and reduction of the spectrograms, leading to tables of intensities for the hydrogen Balmer and Paschen lines, and (2) interpretation of these data, leading to a detailed specification of the thermodynamic conditions of the chromosphere. The work reported in this thesis encompasses the first of these objectives, so far as the data obtained at Khartoum permit, and includes a preliminary interpretation of the results to be expected.

II. OBSERVATIONS AT THE ECLIPSE

The High Altitude Observatory eclipse expedition, a part of the larger expedition of the Naval Research Laboratory, was headed by Dr. John W. Evans,* who was assisted by Mr. Robert H. Lee and Mr. Robert H. Cooper. Observations were made with three slitless spectrographs, two having lens systems and one a reflection system for the image-forming elements. The properties of the spectrographs are given in Table 1.

A diagonal mirror in the ultraviolet spectrograph, between the grating and the spherical mirror, diverted the spectrum to the photographic emulsion. This mirror blocked out 40 mm of the short dimension of the grating, leaving an effective surface of 85 x 150 mm.

All three spectrographs were attached to a single rigid structural spar, mounted equatorially, and guided in hour angle and declination by a photoelectric servo-mechanism[8] similar to those used at the Climax and Sacramento Peak coronagraph stations.

The cameras were designed for "jumping film" observations at a much faster rate than earlier eclipse-goers had attempted. A pneumatic film transport and shutter system was used. This design allowed a rapid film transport with a minimum of mechanical motion or vibration. The cameras used 20-foot rolls of film 9 1/2 inches wide prepared by the Eastman Kodak Company. The spectrum was imaged on the film with the direction of dispersion along the 9 1/2 inch dimension. It was necessary to move the film only about two inches between exposures. The cameras were all operated

---

* Dr. Evans is now Superintendent of the Upper Air Research Observatory at Sacramento Peak, New Mexico.

Table 1

Characteristics of High Altitude Observatory Spectrographs

	Wavelength range	Grating				Image system	Dispersion
		Ruling	Area	Blaze	Ruled by		
Ultra-violet	λ5100 to λ3400	900 lines per mm.	125 mm by 150 mm	λ3700 1st order	Bausch and Lomb	Spherical mirror 60 in. f.l.	7.5 A/mm
Visual	λ6400 to λ3950	600 lines per mm.	100 mm by 150 mm	λ5500 1st order	Bausch and Lomb	Ross lens 4 in. ap. 60 in. f.l.	12 A/mm
Infrared	λ8800 to λ6100	15,000 lines per mm.	125 mm by 160 mm	---	R.W. Wood	Ross lens 4 in. ap. 60 in. f.l.	6.6 A/mm

by a single control system giving simultaneous exposures.

The observing program at eclipse was as follows: the exposure times in the low chromosphere were 0.3 second with an interval of 0.1 second between the end of one exposure and the beginning of the next. The 0.3 second exposures were started 10 seconds before the computed time of first flash. At the appearance of the flash the program control was started. The 0.3 second exposures were continued for 12 exposures, and then four exposures of 0.9 second and four of 2.9 seconds were taken. After the last 2.9 second exposure, some longer exposures of the corona were made. The same program was reversed for second flash. Through some unexplained mechanical peculiarity, the first 0.9 second exposure turned out to be 0.6 second.

The observing conditions at Khartoum were excellent. The sky was cloudless, the wind velocity moderate, and the seeing good. On February 22, there was a cold frontal passage with a rather severe sandstorm. On the day of the eclipse there was still a slight blowing of the sand, but this was confined to the levels a few feet above the surface and below most of the observing equipment. There was still a slight haze left by the dust from the preceding storm. However the atmospheric transparency was good and showed no evidence of being variable. The photopic and spectral attenuation of the atmosphere was measured by the Naval Research Laboratory group[9] during the 10 days preceding the eclipse and on eclipse day.

The expedition was not without serious troubles, however. In the process of setting up and aligning the equipment, Dr. Evans fell from the spar and fractured his leg. This accident seriously jeopardized the expedition, and it was only through extreme effort on the part of all three members of the team that any observations were obtained. In addition to

this, the sandstorm on February 22 forced sand into the film transport and shutter system. The operation of this system afterward was somewhat erratic. Fortunately, the operation during the eclipse was quite smooth, and a relatively large number of excellent spectrograms was obtained. This system failed to operate, however, during the standard exposures taken in Khartoum after the eclipse. Because we had, as a safety measure, planned alternative ways of accomplishing the photometric standardization, the loss of these standard exposures was not so serious as it might, at first sight, appear. This point will be discussed in detail in part III.

Seventeen ultraviolet and 19 visible spectrograms at first flash are of good quality and suitable for accurate photometry. The infrared spectrograms were underexposed, and, although there is much usable information on them, the Paschen lines are too weak for accurate hydrogen line photometry of the desired type on all except one spectrogram. The sand in the pneumatic system produced a few double exposures. In some of the spectrograms there is evidence that the film moved while the shutters were open. This effect shows up as a slight blurring of intense lines, perpendicular to the direction of dispersion. There is no evidence of blurring in the lines of medium intensity, and the actual intensity measurements show that this effect was minor. On the whole the spectrograms at first flash were very good.

The program for second flash started too late, and the longer exposures were overexposed. There are, however, six visible and six ultraviolet spectrograms at second flash that were exposed for 0.3 second in the low chromosphere. These spectrograms were of exceptionally good quality.

The spectrographs were designed so that two images of the spectrum

appeared side by side in each exposure. The two images were accomplished with a simple image-dividing system in each spectrograph. The primary image received practically all of the light from the grating, and the secondary image received approximately 1/100 of the total light. The actual intensity ratio depended on the wavelength, since the reflection and transmission coefficients of the systems varied with wavelength. This simple device greatly increased the amount of usable information on the spectrograms by extending the range of intensities that can be measured. In addition, this system greatly improved the chances of getting usable densities in any given exposure, and it provided a basis for checking the accuracy of the photometry, as described below.

Along with the two images of the spectrum, each exposure contained the image of a data panel. The panel included a step wedge as a check on photometry, and a system of clocks for measuring exposure times. The step wedge was illuminated from behind by a constant light source; the light transmitted by the wedge was filtered to give a band about 400 A. wide.

Plates 1 and 2 are reproductions of visible and ultraviolet spectrograms. The bright regions bordering the primary image were formed by the coronal continuum that extends beyond the moon's limb at right angles to the line of contacts. This continuum overlaps the secondary image of the spectrum and the image of the data panel. In designing the eclipse spectrographs Dr. Evans overlooked the fact that this continuum would be so intense. This oversight had both beneficial and detrimental effects. The overlap into the secondary image raised the densities in that image above the extreme toe of the characteristic curve, making the determination of intensities more reliable, and introduced no systematic errors, since the

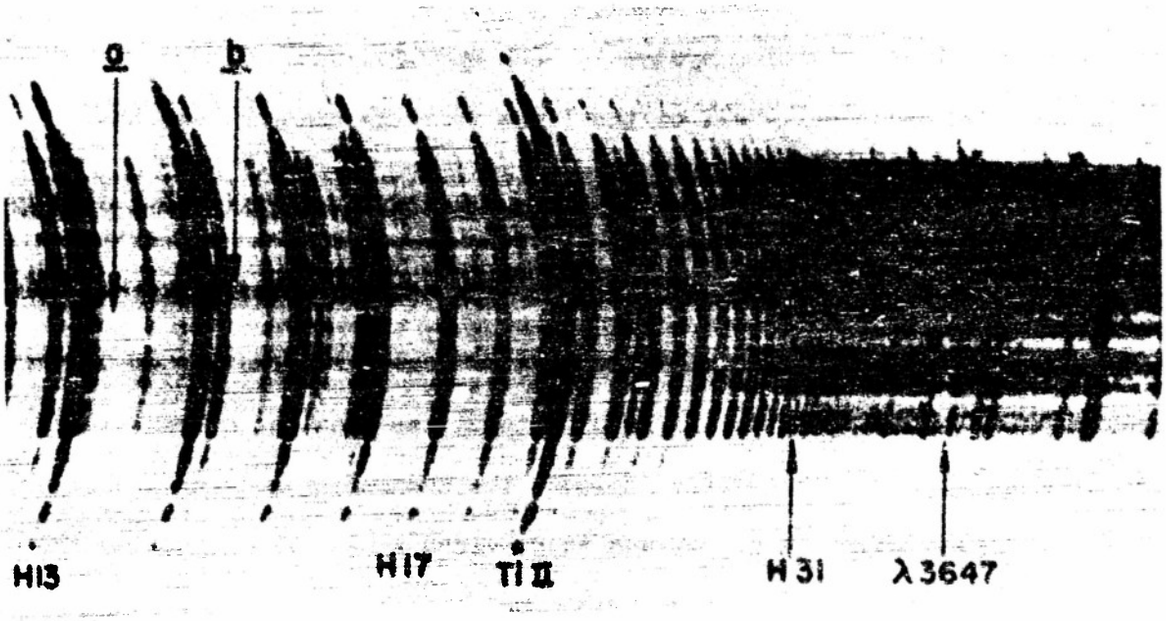

Plate 1. Negative print of a portion of ultraviolet spectrogram No. 9. Points a and b and several Balmer lines are indicated.

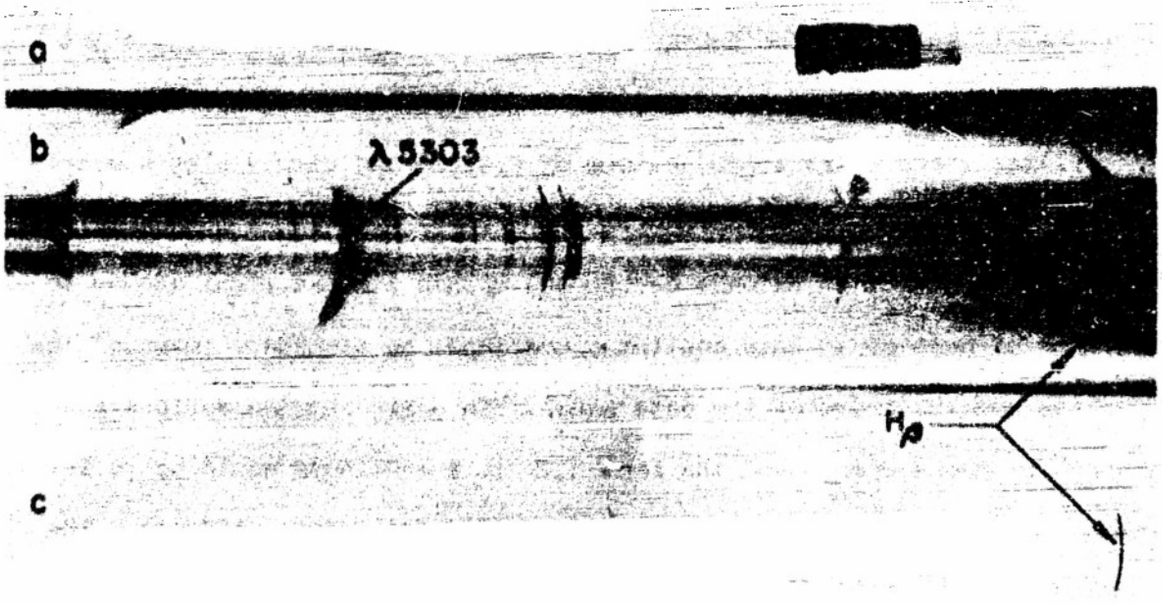

Plate 2. Negative print of a portion of visual spectrogram No. 13 showing: a. data panel wedge; b. primary image; c. secondary image.

light of the overlapped image integrated out of all line intensities in the reduction process. On the other hand, the effects on the data panel were detrimental. In the visible spectra, the effect is scarcely noticeable, and even for the step wedge can be reliably corrected. In the ultraviolet, however, the data panels were of little use. In only six exposures could the clock images be seen, and none of the wedges were usable. At first we feared that this was a very serious loss, but, as we shall point out below, the image of the continuum itself allowed us to determine the characteristic curves of the film at all desired wavelengths, and also to determine the relative exposures of each image.

Prior to these observations the most complete and most useful chromospheric eclipse observations that give reliable intensity measurements are those reported by Cillié and Menzel.[2] They made five observations of the chromospheric spectrum between 0 and 4000 kms. During each of their exposures the moon moved 417 km relative to the sun, and during the interval between the middle of two consecutive exposures the moon moved 833 km relative to the sun.

For comparison, at the Khartoum eclipse we were able to cut the relative motion of sun and moon between exposures to one-eighth of this value. During an interval of 0.3 second the moon moved 81 km and in 0.4 second 108 km relative to the sun. The relative motion of the sun and moon was slower (269 km/sec) and we spaced our exposures much more closely. In the range 0 - 3700 km we have 18 separate observations in the ultraviolet, and each of these contain two images of the spectrum. Were it not for double exposures there would have been a total of 22 spectrograms between these same levels. There can be no doubt that the large increase in the height

resolution in these observations will be of great importance to anyone attempting a study of the chromospheric structure. The accuracy and reliability of the data obtained from the spectrograms will be discussed in the following sections.

III. PHOTOMETRIC METHODS

A. Summary of Planned Photometric Program

Two principal methods of photometric standardization of our eclipse films were planned before the eclipse, with several possible alternatives visualized in case of difficulties with these principal methods. As our program developed, we were forced to rely entirely upon alternatives, but because of the way in which the photometric procedures were executed, as described in detail below, we are confident that the final results, though more laboriously derived, are comparable in accuracy with those expected from the originally planned methods.

Our initial standardization plans called for us to produce a set of standard exposures in our spectrographs, using as a light source a calibrated tungsten ribbon-filament lamp and a collimator of known photometric characteristics. We planned to image the filament of the lamp on the slit of a collimating system like that of Figure 1a, attached to the spectrographs. For the standard exposures we had planned to use a straight slit, covered by a wedge whose transmissivity varied continuously along its length. Thus the image of the slit on the film would be a continuous spectrum with a change of intensity normal to the dispersion. We planned to determine the absolute intensity of the light producing given blackening of the film from the constants of the lamp and the collimating system. The standard exposures we planned to place on the film, adjacent to the eclipse spectra, as soon as possible after eclipse, and to accomplish the processing in the same film strip at the same time as the eclipse films. The principal check on the method was to be the standard wedge in our data

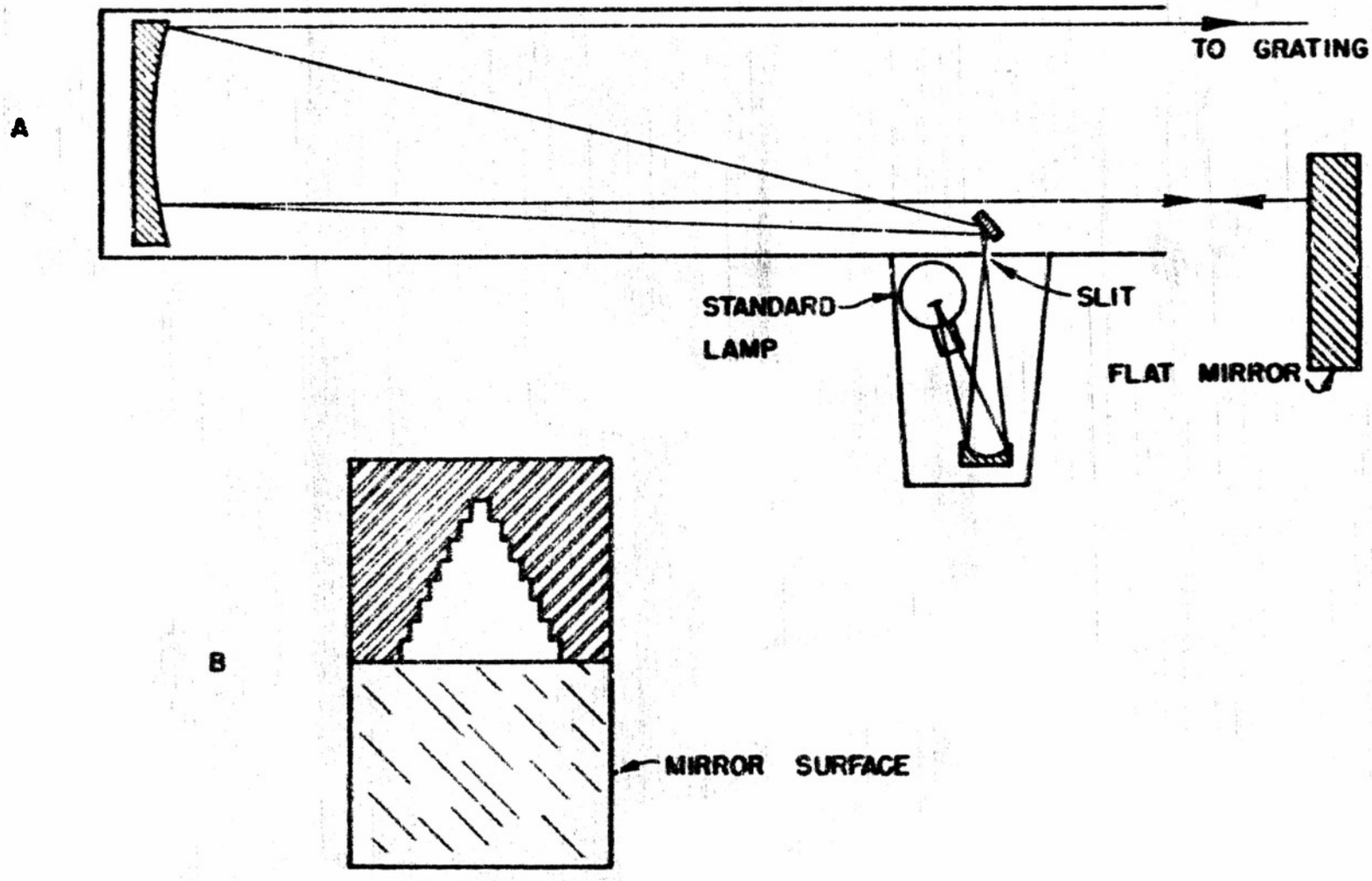

FIG. 1 A - COLLIMATOR B - STEP SLIT

boxes, recorded on each eclipse exposure with the same length of exposure and at the same moment as the eclipse exposure.

Unforeseen difficulties prevented us from carrying out this program, and forced upon us a far more laborious procedure, as described below. We did, however, use the collimating equipment designed for use in the planned procedure, even though simultaneous processing of eclipse and standard exposures made at the time of the eclipse was impossible.

B. Photometric Program as Executed

The planned standard exposures, using the procedures outlined above, were attempted in Khartoum, shortly after the eclipse. For some reason, probably the sand in the system, the film transports failed in all three cameras, and the films of the eclipse spectra, therefore, were not accompanied by these standards, when processed. Another attempt to get the standard exposures was made in Khartoum, but, unfortunately, the expedition had to leave the site so soon that there was neither time nor facilities to process the film until after the return to Boulder. When this film was processed, we discovered that the film transport in the ultraviolet camera had again failed. The visible was partially successful, and the infrared operated normally. However, the long delay between the exposing and processing and the unknown storage conditions, gave us considerable doubt about the accuracy of the standards. The rolls of film that were used for the eclipse spectrograms were still not completely used up. The equipment was therefore reassembled in Boulder and the standard exposures again completed on the same rolls of film. Two sets of standard exposures were taken at different times and processed separately. The processing and

exposing conditions used in Khartoum had been carefully recorded and an attempt was made to duplicate these conditions exactly for the standards taken in Boulder. The same person did the processing in both places. We recognized, however, that the detailed shape of the characteristic curves obtained from these exposures would be only a first approximation to the proper curves, but the variations of the curves with wavelength and the absolute intensity for the middle of the straight line portions of the characteristic curves we expected to be able to trust.

The standard step wedge impressed on the films during the eclipse exposures recorded successfully in the visible spectra, but was obscured in the ultraviolet by the continuum, which overlapped into the area reserved for the data box. The light passing from the wedge to the films was traversed through a green filter that transmitted a band of light about 400 A in width, giving us a characteristic curve at one wavelength.

The image divider, which gave two images of the spectrum on each exposure also aided us materially in checking the photometry as outlined below.

C. Method of Determining Characteristic Curves by Standard Lamp and Collimator

The method used in Boulder to standardize the photographic films exposed to the standard lamp and collimator was exactly the same as that originally planned for the eclipse films themselves. Because the films had to be developed separately from the eclipse films, and in spite of the fact that the same emulsions were used and conditions were duplicated as closely as possible, we used the characteristics so derived simply to give

us a first approximation to the appropriate curves, to determine the wavelength variations of the curves, and to fix the absolute intensities corresponding to the middle of the straight line portions of the characteristic curves.

The method gives absolute characteristic curves for the films at all desired wavelengths. The first step in the method is to obtain an expression for the absolute intensity of a chromospheric spectrum line in terms of the characteristics of the standard lamp and collimator. This we have done in the following steps, leading up to equations (8) and (9) on page 17.

The lamp we used was calibrated by the National Bureau of Standards before the standard exposures were taken. After the entire expedition and post-expedition standardization had been completed we had the lamp recalibrated. We found that no important change in the characteristics of the lamp occurred. The calibration gave the brightness temperature of the lamp for several values of the filament current. The brightness temperature, $S\lambda$, is related to the true temperature, T, through the equation

$$\frac{1}{T} = \frac{2.303\ \lambda\ \log \epsilon_{\lambda T}}{c_2} + \frac{1}{S\lambda} \qquad (1)$$

where $C_2 = 1.432$ cm degrees and $\epsilon_{\lambda,T}$ is the spectral emissibity of tungsten. The values of $\epsilon_{\lambda,T}$ given by Forsythe and Adams[10] were used. The intensity of the radiation from 1 cm^2 of the filament, expressed in terms of the black body emission function, $J_{\lambda,T}$, in ergs/sec/unit solid angle/unit wavelength is

$$E_{\lambda T} = \epsilon_{\lambda T}\ J_{\lambda T}. \qquad (2)$$

Let:

ρ_λ = the average coefficient of reflection at wavelength λ, of the six reflecting surfaces in the collimator and ultraviolet spectrograph.

$\tau_{\lambda,x}$ = the transmissivity of the wedge at a distance x from the end of the slit and wavelength λ.

Ω_g = the solid angle subtended by the grating as seen from the slit.

ω_s = the width of the slit.

Then the intensity in ergs/sec/unit wavelength which reached an area, $d\ell\, d\lambda$ of the film in the ultraviolet spectrograph from a length of slit, dL, located at the distance x from one end of the slit is

$$\epsilon_{\lambda,T}\, J_{\lambda,T}\, \rho_\lambda^6\, \tau_{\lambda,x}\, \Omega_g\, \omega_s\, dL. \qquad (3)$$

The intensity of radiation in ergs/sec/unit wavelength from the chromosphere which reached the same area of film is

$$\frac{d\mathcal{E}_c\, \omega_g\, L\, \rho_\lambda^3}{4\pi\, d\ell_\lambda}\, e^{-\beta_\lambda} \qquad (4)$$

where:

$d\mathcal{E}_c$ = ergs/sec in wavelength range $d\lambda$ emitted uniformly in all directions by a section of the chromosphere bounded by two parallel planes lying in the line of sight, 1 cm apart, and perpendicular to the sun's limb, and a third plane tangent to the moon's limb along the line of sight.

ω_g = the solid angle subtended by the grating as seen from the sun.

L = the length of the chromospheric section which is imaged with a length $d\ell$ on the film.

β_λ = the spectral attenuation of the atmosphere.

Equating (3) and (4), we get

$$d E_c = 4\pi e^{\beta\lambda} \frac{\Omega_g}{\omega_g} \frac{dL}{L} \omega_s \rho_\lambda^3 \tau_{\lambda,x} \epsilon_{\lambda,T} J_{\lambda,T} d\lambda . \qquad (5)$$

The ratio of the solid angles subtended by the grating from the two sources is equal to the reciprocal of the ratio of the effective distances squared. The effective distance of the grating from the slit is equal to the focal length of the collimator, f_c. If we call the distance from the sun to the earth R, then

$$\frac{\Omega_g}{\omega_g} = \frac{R^2}{f_c^2} . \qquad (6)$$

The ratio of the length of slit to the length of the chromospheric section that has the same image size is equal to the ratio of the magnification, or the ratio of the effective distances. Hence,

$$\frac{dL}{L} = \frac{f_c}{R} . \qquad (7)$$

From (6), (7) and (5), we get

$$\frac{dE_c}{d\lambda} = 4\pi e^{\beta\lambda} \frac{R}{f_c} \omega_s \rho_\lambda^3 \tau_{\lambda,x} \epsilon_{\lambda,T} J_{\lambda,T} . \qquad (8)$$

The total energy emitted in a line is the integral of (8) over the line profile, or

$$E_c = 4\pi \frac{R}{f_c} \omega_s \int_{\lambda_1}^{\lambda_2} e^{\beta\lambda} \rho_\lambda^3 \tau_{\lambda,x} \epsilon_{\lambda,T} J_{\lambda,T} d\lambda . \qquad (9)$$

The next step in the method is to evaluate the properties of the collimator, represented by terms ρ_λ and $\tau_{\lambda,x}$. $\epsilon_{\lambda,T}$ is already known as mentioned above, from published values.[10] β_λ, the spectral attenuation

comes from Naval Research Laboratory data already described.[9] All the other terms are known.

In order to evaluate ρ_λ we used a special slit. The upper half of this slit, as shown in Figure 1b, had eight steps whose widths varied logarithmically. The lower half was a mirror surface. Light from the upper half of the slit formed a collimated beam. A flat mirror placed in this beam, as shown in Figure 1a, reflected part of the collimated beam back into the collimator, and formed an image of the upper half of the slit on the mirror surface of the lower half of the slit. Light from this image then returned to the collimator mirror. Hence a portion of the beam emerging from the collimator contained light from both the upper half of the slit and its image on the lower half. Only this portion of the beam was allowed to strike the grating. The image on the film consisted of two separate continuous spectra with the intensity varying in steps normal to the dispersion. One of the spectra was formed by the image of the slit which had been reflected from three surfaces in the collimator. The other spectrum was formed by the image of the slit which had been reflected from nine surfaces in the collimator. The range of intensities is such that the intensities in the two images overlap. At points of equal density, at the same wavelength, the intensities are the same in the two images. The intensity which produces this density is proportional to $W_s \rho_\lambda^n$, where n is the number of reflecting surfaces and W_s is the width of the slit. If we denote the multiply reflected image by primes, we have

$$W_s \rho_\lambda^3 = W_s' \rho_\lambda^9 \qquad (10)$$

or

$$\rho_\lambda^3 = \left(\frac{W_s}{W_s'}\right)_\lambda^{1/2} \tag{11}$$

thus giving us the desired evaluation of ρ_λ^3.

It should be noted that this method assumes that the two reflections occurring at the flat mirror in the collimated beam and the mirror surface on the slit are equivalent to two reflections from the focusing mirror in the light house. All of the reflecting surfaces were coated with the same material at the same time. Any differences in the reflection coefficients should be due to contamination of the surfaces and we believe that such differences were negligibly small.

To evaluate $\tau_{\lambda,x}$ we compared the exposures from the step slit with exposures from the wedge-covered straight slit. The exposure times and lamp temperatures were the same. From the image of the step slit we plotted a curve of density vs. log W_s, as shown in Figure 2b. The lower half of this curve was obtained from a set of exposures taken with a smaller aperture in the collimated beam. The middle portion of the curve was obtained from the multiply-reflected image with the large aperture. The densities in the multiply-reflected image were plotted at a point on the abscissa corresponding to $\log W_s + 6 \log \rho_\lambda$. From the image of the straight slit and wedge, we plotted a curve of density vs. the distance, x, from the end of the slit, as shown in Figure 2a. At points of equal density on the two curves, the intensities are equal. The intensity in the image of the step slit is proportional to W_s, and the intensity in the image of the straight slit and wedge has the same proportionality to $w_s \tau_{\lambda,x}$. Hence,

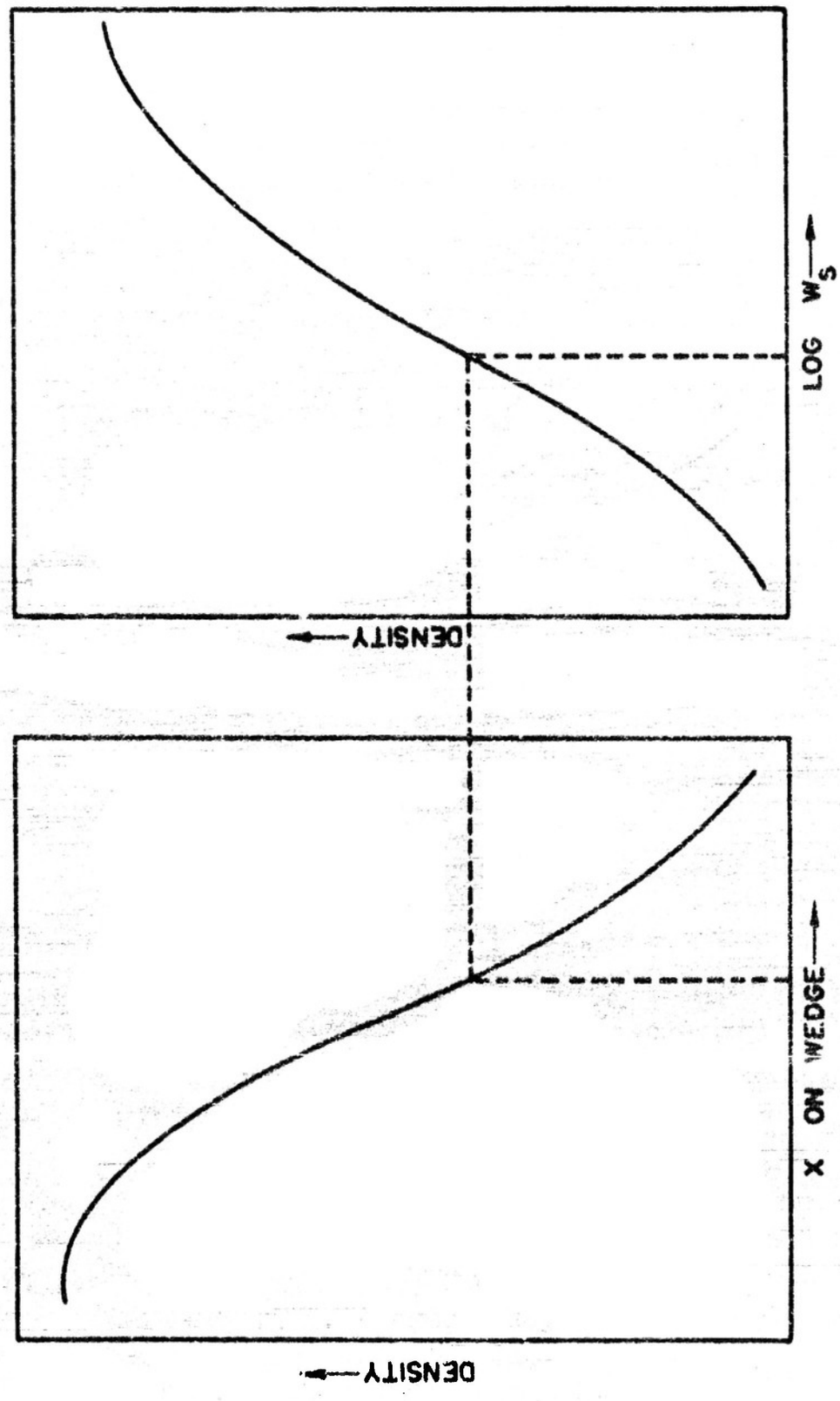

FIG. 2 A-DENSITY VS DISTANCE ALONG WEDGE B-DENSITY VS SLIT WIDTH

$$\tau_{\lambda,x} = \left(\frac{w_s}{w_s}\right)_{\lambda,x} . \qquad (12)$$

w_s is a constant. At a point on the wedge a distance x from the end of the slit the density can be read from the curve in Figure 2a. At the same density on the curve in Figure 2b the value of W_s is determined. Both curves have been plotted at each wavelength where values of ρ_λ and $\tau_{\lambda,x}$ were desired. Each curve is based on the average densities measured on five separate exposures which were supposed to be identical, but which show slight variations due to various photographic defects.

We have now reduced ρ_λ and $\tau_{\lambda,x}$ to known measurable quantities. The values of β_λ, ρ_λ and $\tau_{\lambda,x}$ and the optical constants of the lamp for the wavelengths λ3900, λ3800, λ3700, λ3600, and λ3500 are tabulated in Table 1 in the Appendix. The values of $\log\left(\frac{dE_s}{d\lambda}\right) = \log\left(\pi r e^{\beta_\lambda} \frac{f}{f_1} w_1 \rho_\lambda^2 \tau_{\lambda,x} \epsilon_{\lambda,T} J_{\lambda,T}\right)$ and the densities* for values of λ and x, on the two sets of 0.3 second standard exposures are tabulated in Tables 2 and 3 in the Appendix. Each density recorded is again the average of the densities from five separate exposures. The values of x marked with a prime in Tables 2 and 3 refer to exposures taken with a filament current of 30 amps. The unprimed values are for exposures with a filament current of 36 amps; the higher current being used to obtain more light.

We now have all necessary information to draw an absolute characteristic curve for our film at any desired wavelength for the 0.3 second exposures. We do this by simply plotting the measured densities for any

---

* All densities used in this report are American Standard diffuse densities unless otherwise specified.

given λ and x against the calculated value of $\log \left(\frac{dEc}{d\lambda}\right)$ given in the tables.

From this characteristic curve, thus, if we enter measured chromospheric or coronal densities at any given wavelength we can read directly the corresponding absolute intensity per unit wavelength. By integration we can obtain the desired total line intensities from measured line profiles.

If these characteristic curves accurately represented our eclipse films, the eclipse photometry would simply represent application of this technique. However, the main labor of our photometric problem was to obtain from less direct information characteristic curves that did represent the eclipse films.

We encountered some perplexing difficulties as a result of comparison of the two different lamp intensities corresponding to the different lamp currents used. In the 0.3 second exposures two different currents, 30 and 36 amps, were used. The 30 amp exposure gives the lower part of the characteristic curve and the 36 amp the upper part. In the two sets of exposures there is a good overlapping of the densities in the straight line portions of the characteristic curves. The observed difference between the values of $\log \left(\frac{dEc}{d\lambda}\right)$ at equal densities on the two sets of exposures does not agree with the difference that is calculated from the Planck function and the value of $\epsilon_{\lambda,T}$ and T. In all cases the calculated differences is greater than the observed difference. The amount of this residual is entered in the last rows of Tables 2 and 3 in the Appendix. The values of $\log \left(\frac{dEc}{d\lambda}\right)$ entered in the tables for the 36 amp exposures are the computed values minus one half of the residual, and the values for the

30 amp exposures are the computed values plus one-half of the residual. The residuals seem to change with wavelength, in opposite directions in the two sets of standards, and the average values are different for the two sets. The changes with wavelength are too small to be considered significant, but the change between the average value for the two sets is significant.

This same sort of trouble shows up when the 0.9 second and 2.9 seconds exposures are compared to the 0.3 second exposures. The 2.9 seconds exposures were taken at 30 amp and the 0.9 second at 33 amps. The difference between the values of $\log\left(\frac{dEc}{d\lambda}\right)$ for the 0.9 second exposures and 0.3 second exposures is not the same in the two sets of standards. The difference is again of the order of 0.10 in $\log\left(\frac{dEc}{d\lambda}\right)$. The 2.9 seconds exposures in set B showed an obvious non-uniform illumination of the slit. The discrepancies are too large to attribute to errors in the lamp constants. The two independent calibrations of the lamp gave consistent results and the current in the filament was controlled to $\pm$ .01 amps. The values of $\epsilon_{\lambda,T}$ that have been reported[10, 11, 12] show considerable variation in this wavelength range but not nearly enough to explain the differences. The fact that the two sets of exposures show the same trends in the 0.3 second exposures but opposite trends in the comparison of the 0.3 second to the 0.9 second exposures also argues against the suggestion that the constants are the source of trouble.

The only other possibility is a non-uniform illumination of the slit. There is one obvious case of this and there is a chance that it is the cause of all the discrepancies. When the current in the filament changes, the filament expands or contracts, and in doing so, it changes its position. It is possible that these changes are enough to cause significant changes in

the position of the image of the filament. The slit was nearly as wide as the filament, and a small motion of the image could be quite serious. The image may also have been moved by mechanical disturbances. In order to change the exposure times it was necessary to remove the housing that held the lamp and the focusing mirror. After each change, the position of the filament image on the slit was checked before the final adjustments were made. The one obvious case of non-uniformly illuminated slit, however, leaves this as a strong possibility. The results of these discrepancies are that the absolute intensity scale is uncertain to ± 0.10 in the log of the intensity and that the relative intensities between the different exposure times are unreliable. Fortunately, the image of the coronal continuum on the spectrograms offers a means of getting the relative intensities between the various exposures, so this trouble is not serious.

D. Method of Determining Characteristic Curves by Use of the Coronal Continuum and the Data Panel Wedge

As pointed out earlier, we consider the shape of the characteristic curves obtained from the above standards to be no more than a first approximation to the true curves of the eclipse films, and, indeed, the two sets show curves of slightly different shape. The variations of the curves with wavelength we consider to be reliable, and they are the same in the two sets. The absolute intensity scale at the middle of the straight line portion of the curves should be reliable to ± 0.10 in the log of the intensity. Fortunately, due to the standardizing methods used at the eclipse, the shape of the true eclipse characteristic curve at one given wavelength can be determined entirely independently of the standard exposures of the above section.

If the data panel wedge on the ultraviolet spectrograms had been usable, this approach would have been straightforward. Since no ultraviolet wedges were usable, the approach was indirect; we used one of the two available alternatives for building up the characteristic curves.

One procedure is to consider each pair of corresponding points in the two images (one strong and one weak) of each spectrogram as a wedge of two steps. This multitude of wedges can then be combined to give the equivalent of a wedge with many steps. This procedure is complicated by the irregular operation of the shutters, the large ratio of intensities between the two images, and the superposition of the coronal continuum from the primary image on the secondary image. These complications make the determination of the characteristic curve by this method very difficult and laborious.

The other alternative is to use the data panel wedge on the visible spectrograms to determine the characteristic curve at one wavelength for the visible film, and then to use this curve to construct the curves for the ultraviolet films. This procedure is not nearly so impossible as it might seem. The spectral region λλ 5100-3900 is common to both visible and ultraviolet spectrograms, and the transmission range of the filter used in the formation of the image of the step wedge was λλ 5200-4700. The wedge then gives a characteristic curve accurate in the vicinity of λ4900. We can use this curve to determine the relative peak intensities of several lines near this wavelength on a given visible spectrogram. These same lines on the ultraviolet spectrogram exposed at the same time then serve as a step wedge from which the characteristic curve at λ4900 on the ultraviolet spectrograms can be obtained. The random errors would be large, but there are enough pairs of spectrograms and enough lines to average out

these errors safely.

Another method of transforming this characteristic curve for the visible spectrograms into the characteristic curves for the ultraviolet spectrograms was suggested by Dr. Evans. The coronal continuum bordering the darker image of the spectrum is an outstanding feature of both the ultraviolet and visible spectrograms. The importance of this continuum was not fully realized in the design of data panel system, and, as a result, the step wedge and most of the clock images in the ultraviolet were completely useless. At first sight it appeared that the continuum had almost completely destroyed any hope of getting an accurate characteristic curve for the ultraviolet spectrograms. Further consideration, however, showed that the continuum is extremely valuable, both as a means of getting the characteristic curves, and as a means of comparing intensities in the different exposures.

Each monochromatic image of the eclipsed sun would show as a ring of light, looking something like the image of the green, $\lambda 5303$, corona on the visible spectrogram in plate 2. When these images are dispersed, along the line of contact, each point in the spectrogram receives light from all of the overlapping images. Along the line of contact the dispersion is normal to the sun's limb, and the effect of the overlapping images is relatively small. At points on the moon's limb $\pm 90^{\circ}$ from the line of contact the dispersion is parallel to the limb. In this case the effect of the overlapping images is pronounced. The net result is an intensity distribution in the continuum normal to the dispersion similar to that shown in Figure 3. The intensities inside the moon's diameter change during the eclipse, reaching a minimum near the middle of totality.

Outside of the moon's diameter the intensities are independent of the position of the moon, and during the short time of the eclipse they should be constant. The fact that this source is constant throughout the eclipse, and that it is a continuous spectrum of known spectral character, as described below, renders it a suitable standard by means of which we can transpose the characteristic curve at λ4900. to any desired wavelength.

Since the line of dispersion is along the line of contacts, the maximum at the edge of the moon is the same distance from the center of the sun in all of the spectrograms, and it can be used as a convenient reference point. The intensity at a given point in the image of the spectrogram is the sum of the intensities from the overlapping images. The intensity contributed at each wavelength is the integral of the monochromatic intensity along the line of sight at a point in the image of the corona which is represented by the point on the spectrogram. Since this point on the spectrogram is at a different position relative to each wavelength, each wavelength is represented by a different region of the corona. The complex nature of this image does not seriously limit its usefulness, however.

The intensity at any point in this image of the continuum depends only on the intensity distribution in the corona and the dispersion of the spectrograph. Both theory[13] and observation[14] indicate that the coronal continuum is, except for absorption lines, a reproduction of the photospheric continuum. In the inner corona it arises from scattering by free electrons, and in the outer corona it arises from scattering and diffraction by larger dust particles. Regardless of its origin, however, the observations indicate that the continuum is the same color at all heights. This, of course, implies that the continuum intensity is the same function of

wavelength at all points in the corona. If this is true, then the ratio of the intensities at two points at a given wavelength in the image of the corona is the same as the ratio of intensities for two points at the same heights from the edge of the moon at any other wavelength, regardless of the dispersion of the spectrograph. If the intensities in this image of the corona can be measured at one wavelength on any spectrogram, then the image can be used as a continuous wedge from which part of the characteristic curve can be obtained at any wavelength on any of the spectrograms where the image is dark enough to be of use.

In particular, we can use the characteristic curve obtained from the data panel wedge on the visible spectrograms to measure the relative intensities as a function of the distance from the maximum in the image of the corona at λ4900 on the visible spectrograms. These relative intensities can then be used to plot the characteristic curves for the ultraviolet spectrograms at any desired wavelength from microdensitometer tracings of the continuum at that wavelength.

The image of the step wedge in the data panel on the visible spectrograms is in the outer edge of the coronal continuum. The intensity in the image of the corona is negligibly small compared to the intensity from the high transmission end of the wedge, but on the low transmission end of the wedge it is a large percentage of the total intensity. In order to get an accurate characteristic curve from this image of the wedge the contribution of the continuum must be evaluated. It is possible to do this by comparing the images of the wedge in any two of the 0.3 second, 0.6 second, 0.9 second and 2.9 seconds exposures. The total intensity of the light at a given step in the wedge is

$$I_i = I_o\, 10^{-\delta_i} + I_c \tag{13}$$

where I_o is the intensity of the light illuminating the step wedge, δ is the green specular density of the step and I_c is the intensity of the continuum. For an image with a different exposure time the same density will be found at a different step. This density is produced by an intensity

$$I_i' = I_o\, 10^{-\delta_i'} + I_c \,. \tag{14}$$

If we let a represent the ratio of the exposure times corrected for the reciprocity failure, then

$$I_i' = a\, I_i \,.$$

Solving these three equations for a, we get

$$a = \frac{10^{-\delta_i'} + I_c/I_o}{10^{-\delta_i} + I_c/I_o} \,. \tag{15}$$

Equation (15) can be written for any density which is in the range covered by both exposures. If we choose a second point, then,

$$a = \frac{10^{-\delta_k'} + I_c/I_o}{10^{-\delta_k} + I_c/I_o} \,. \tag{16}$$

From (15) and (16), we get

$$\frac{I_c}{I_o} = \frac{10^{-\delta_i'}\,10^{-\delta_k} - 10^{-\delta_k'}\,10^{-\delta_i}}{10^{-\delta_k'} - 10^{-\delta_k} + 10^{-\delta_i} - 10^{-\delta_i'}} \tag{17}$$

The value of $\frac{I_c}{I_o}$ is quite sensitive to errors in the quantities $(10^{-\delta_i} - 10^{-\delta_i'})$, but it can be determined for a large number of points

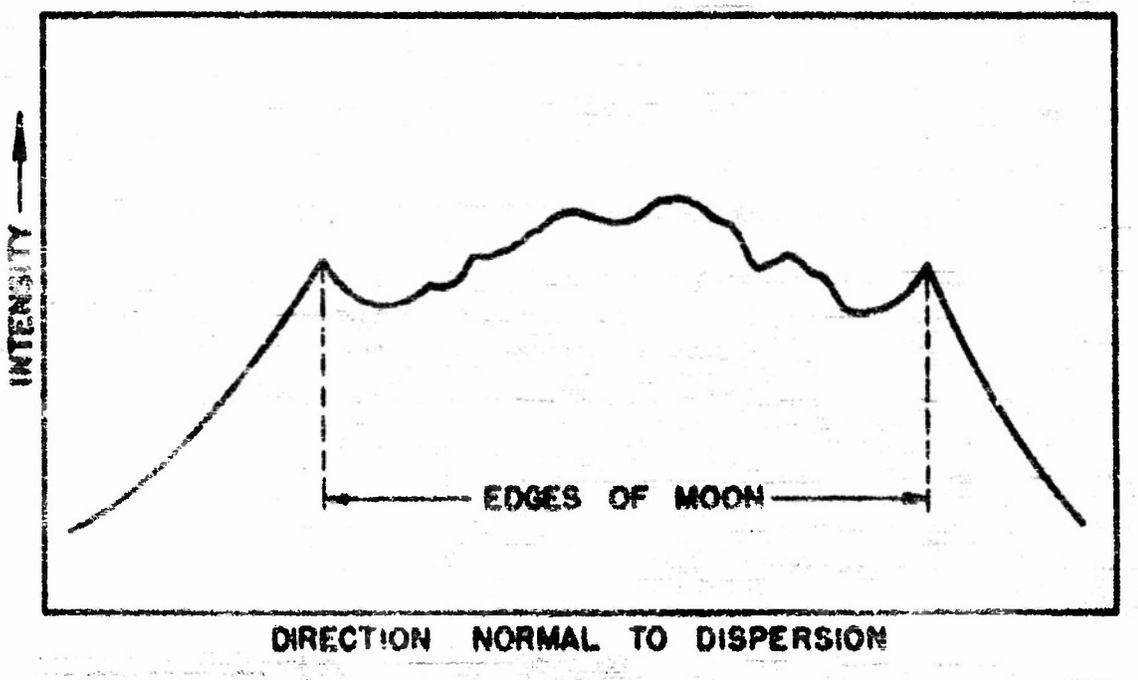

FIG. 3 VARIATION OF INTENSITY NORMAL TO DISPERSION

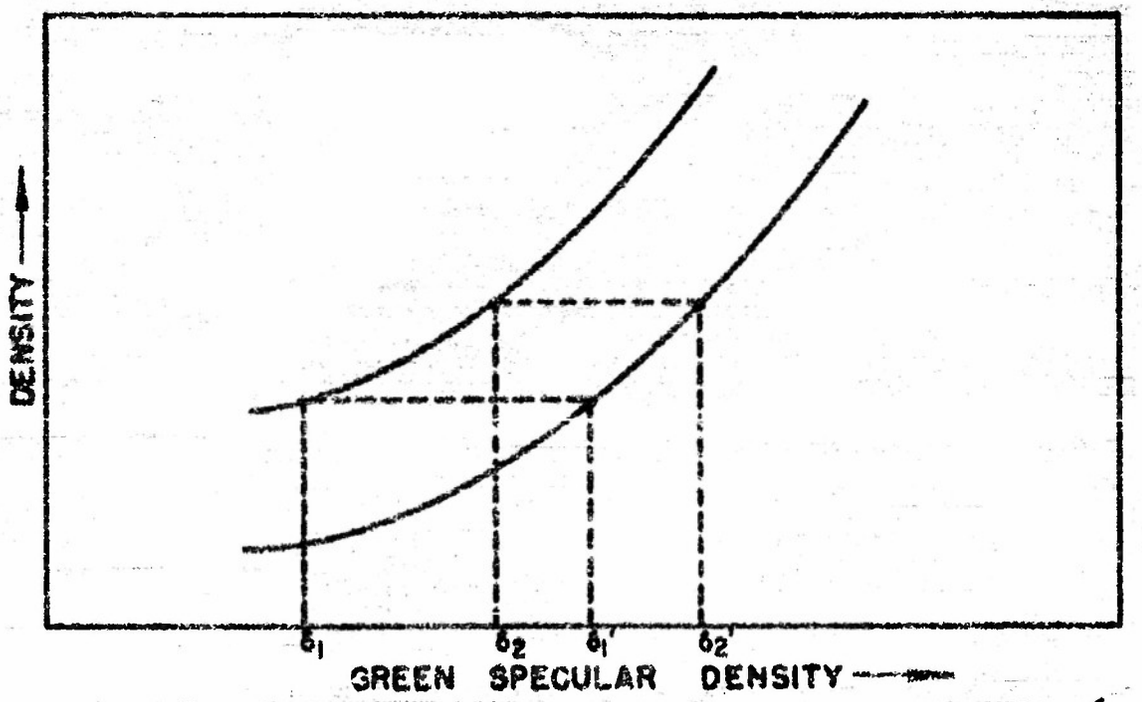

FIG. 4 ILLUSTRATION OF METHOD OF COMPUTING I_c / I_o FROM IMAGES OF DATA PANEL WEDGE IN VISIBLE SPECTROGRAMS.

and the average value used. Equation (17) assumes that I_c is constant throughout the length of the wedge. Measurements of the continuum at the two ends of the wedge show that this is very nearly so. Equation (17) also assumes that $\frac{I_c}{I_o}$ is the same on all spectrograms. The lamp current was accurately controlled, and therefore, I_c is considered constant. It was pointed out above that I_o is also constant.

Figure 4 illustrates the method of computing $\frac{I_c}{I_o}$. The diffuse densities in the steps of two of the images of the wedge with different exposure times are plotted against the green specular densities of the steps on the original wedge. At two pairs of points of equal density on the two curves the values of $10^{-\delta}$, $10^{-\delta'}$, $10^{-\delta_4}$ and $10^{-\delta'_4}$ can be read, and $\frac{I_c}{I_o}$ computed from equation (17). The average value of $\frac{I_c}{I_o}$ obtained from 15 determinations, is 0.036 ± 0.001. In calculating $\frac{I_c}{I_o}$ we used pairs of points which covered both large and small differences in density. We obtained the final curve by plotting the diffuse densities of the steps in the wedge image as ordinates and $\log (10^{-\delta} + \frac{I_c}{I_o})$ as abscissae. The plots from the different exposures are combined into a single curve. The data for this curve are in Table 4 in the Appendix.

When the curves from the different exposure times are combined, the overlapping portions agree very well. This would not be the case if the value of $\frac{I_c}{I_o}$ was in error by any significant amount because the overlapping part of the curve from the shorter exposure is independent of $\frac{I_c}{I_o}$, and the overlapping part from the longer exposures is very sensitive to the value of $\frac{I_c}{I_o}$.

Microdensitometer tracings were made of the coronal continuum at λ4900 on seven of the visible spectrograms which showed no signs of blurring

or fogging. The relative intensities obtained from these tracings and the visible characteristic curve are entered in Table 5 in the Appendix. The values for the seven spectrograms were averaged, and the averages plotted against height. The average value was then given small corrections to make the points follow a smooth curve. Both the averages and the smoothed averages are in Table 5.

The individual intensities for each pair of heights obtained from the spectrograms do not show significantly large departures from the mean. The scatter is well within the limits of the accuracy of photographic photometry. The relative intensities on the spectrograms of different exposure times are based on different regions of the visible characteristic curve, and, in fact, include all of the curve up to density of 1.85. The fact that the values are relatively constant throughout the whole range of exposures indicates that the visible characteristic curve is not significantly in error.

Microdensitometer tracings of the coronal continuum on the ultraviolet spectrograms were made at λ3900, λ3800, λ3700, λ3600, and λ3500. λ3700 was traced on all of the spectrograms, and the others on three spectrograms. The densities obtained from these tracings are tabulated in Table 6 in the Appendix. The images of the moon on the ultraviolet and visible spectrograms are the same size, and the relative intensities measured in the visible apply to points the same distance from the edge of the moon in the ultraviolet continuum. The band of continuum between the two images of the spectrum was used on both the visible and ultraviolet plates. The continuum on the opposite limb of the sun was avoided because the standard exposures showed evidence of vignetting near the edges of the film gate in the

ultraviolet camera. The continuum between the two images is in the center of the exposure where it is free from any danger of vignetting, and less apt to be affected by irregular shutter action. The continuum from the portion of the secondary exposure inside of the moon's diameter is added to this continuum. However, the intensity in the secondary exposure is only about 1% of the intensity in the primary exposure; since only relative intensities are used, it largely cancels anyway. The continuum in the outside edge of the secondary exposures is below the threshold sensitivity of the films.

The section of the curves from the various spectrograms are combined into a single curve at each wavelength by shifting the curves at constant density until they overlap. The tracings at λ3450 and λ3550 were used to aid in drawing the toe of the curves. The highest densities in the continuum are about 2.45. The strong chromospheric lines on the primary image exceed this density. In order to extend the upper end of the curves we measured the relative intensities at the peaks of several of the Balmer lines, from microdensitometer tracings of the secondary images on the spectrograms and the previously determined portion of the ultraviolet characteristic curves at the same wavelengths. We then plotted the densities of the peaks of the same lines at the same point on the limb in the primary image against the logarithm of the relative intensities obtained from the secondary image. This portion of the curve was then shifted at constant density until it joined the other curve. The two sections of the curve joined smoothly. If the previously determined portion of the curve was of the wrong shape, the two sections would not have had the same slope where they joined, and they would not have joined smoothly. The data for the top of the λ3700 curve

are shown in Table 7 in the Appendix. The top of the λ3900 and λ3800 curves were assumed to be parallel to the λ3700 curve. Actually, this portion of the curves was not needed, because the stronger lines were also recorded in the secondary images.

Figure 5 is a plot of the characteristic curves obtained at five wavelengths in the coronal continuum. To avoid confusion only the points for the λ3700 curve have been plotted. The relative positions on the log scale have been determined from the standard exposures.

In Figure 6 the two sets of standards and the coronal continuum curves at λ3700 are compared. The differences between sets A and B indicated the extend of our failure to duplicate conditions on two relatively close occasions at Boulder, and suggested that our chances of duplicating the conditions at Khartoum were not very good. Nevertheless, except for the low density end of the curves, the general agreement was exceptionally good. There cannot be much doubt about the shape of the curves above a density of 0.5, and they all show the same changes in shape with wavelength. The only region where the curves from the coronal continuum required an additional confirmation was below densities of 0.5.

Fortunately, this was not hard to do. It has already been pointed out that when the low density end of these curves was used to construct the high density end of the curves from the two images of the spectrum a very good fit was obtained. If, on the other hand, we did the same thing with the characteristic curve from the standard exposures made in Boulder, the upper end of the curve obtained was much too steep to join the previously determined lower end. As soon as the Boulder standards were completed we suspected some such trouble because the clear film densities on the eclipse

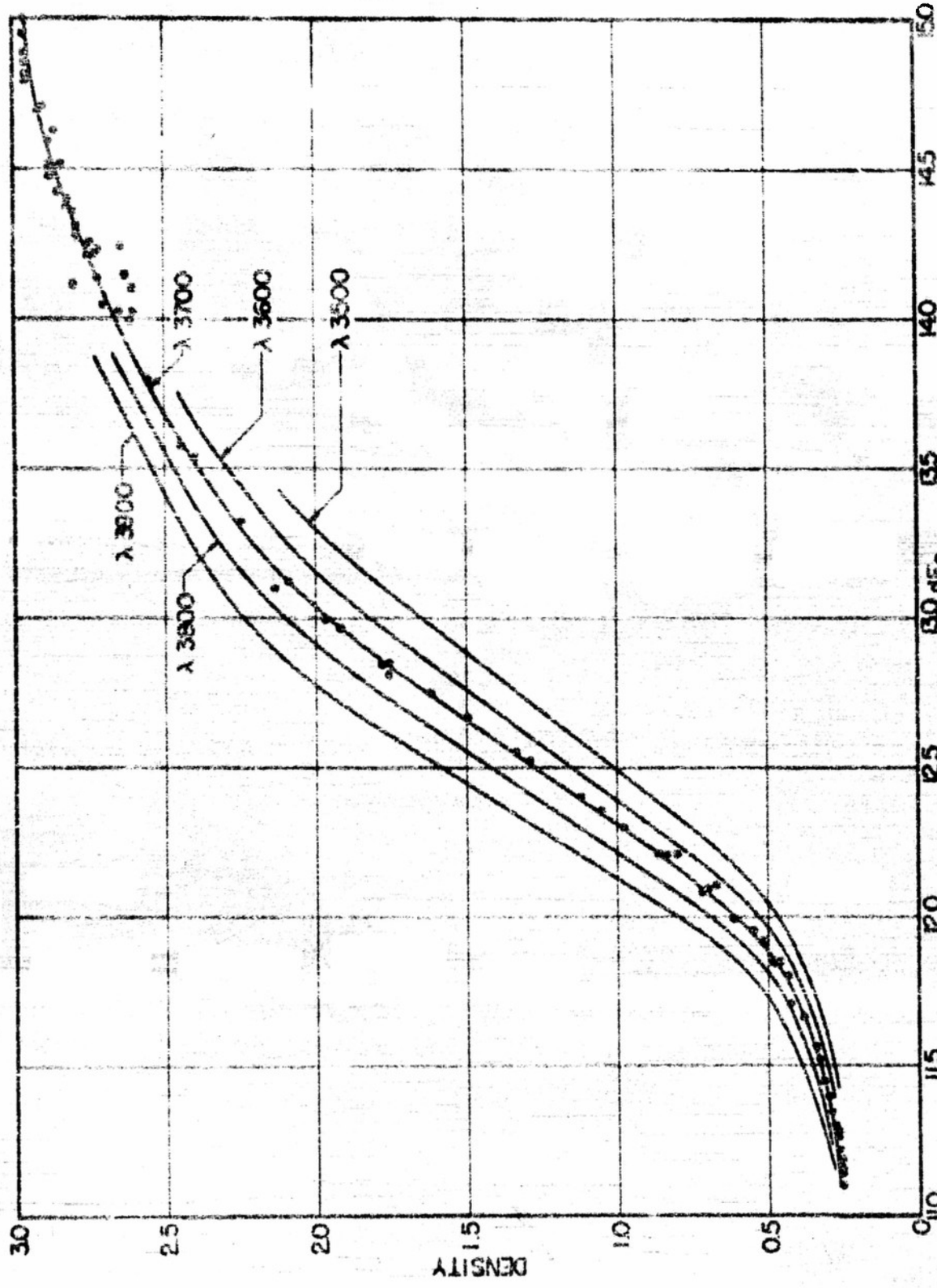

FIG. 5 ULTRAVIOLET CHARACTERISTIC CURVE FROM CORONAL CONTINUUM

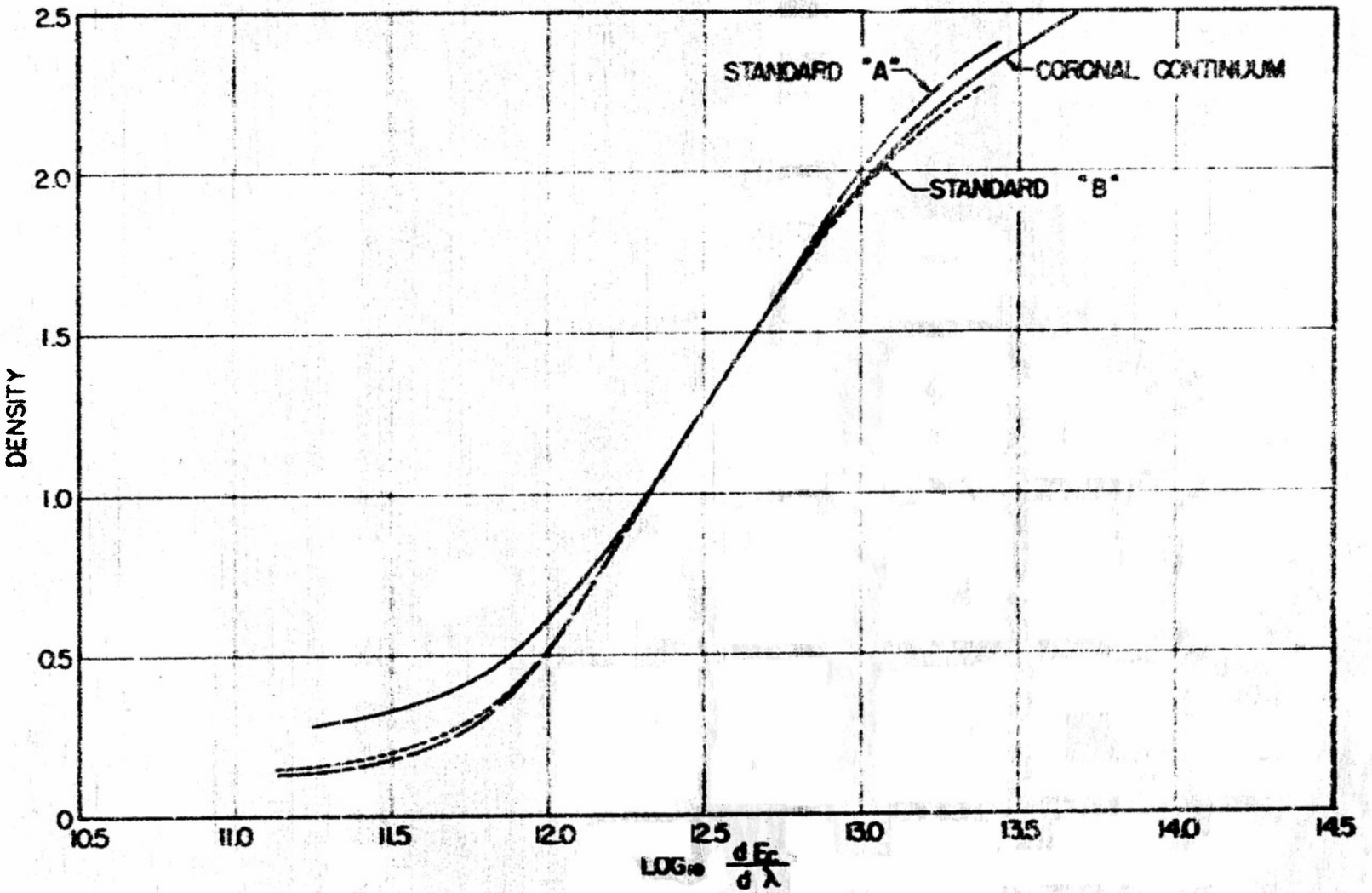

FIG. 6 COMPARISON OF CORONAL CONTINUUM CURVE WITH STANDARDS

films in unexposed regions was 0.23, whereas the clear film densities in the Boulder standards was only 0.14. The same results were found in the visible spectrograms. This is a larger difference than one would expect from processing alone, and there is no evidence in the spectrograms of enough scattered light to cause it. It may perhaps have resulted from differences in the physical conditions of the film at the two times or from some sort of chemical fogging. In any event, the toe of the curves from the Boulder standard exposures was much too low, and the curves from the coronal continuum seem to be approaching asymptotically to a value very close to the eclipse clear film value of 0.23. Another argument supporting the validity of the toe of the curves from the coronal continuum is that the method used to construct the curves requires that if the toe possessed too low a slope, so also would the straight line portion. However the straight line portion agreed very well with that determined in the Boulder standards.

The absolute intensity scale for the characteristic curves obtained from the coronal continuum was determined by matching the straight line portion of these curves with the straight line portion of the standard Boulder exposures derived as described in the previous section. Since the processing and exposing conditions were well controlled, this matching of the curves should not have introduced any significant errors. The curves plotted in Figure 5 include corrections for atmospheric absorption, differential film sensitivity, and differential reflectivity from the mirror surfaces.

The characteristic curves thus derived are exactly comparable with those we would have obtained if the standardization process had operated as initially intended. We believe that these curves are fully as reliable as any we might have obtained by the more direct method, had it succeeded.

IV. TABULATION OF INTENSITIES

The densities in the primary images of the ultraviolet spectra range from 1.2 to 3.0. In the secondary image the densities range from 0.26 to 3.0. The film characteristics are such that the photometry is reasonably reliable up to densities of about 2.8. None of the common commercial microdensitometers will give an accurate measure of such high densities with a reasonable slit size and speed. The microphotometer which has been built for this purpose at the High Altitude Observatory will do this in a very satisfactory manner, but it was necessary for us to do part of the reduction work before this instrument was completed. The only other instrument which, to our knowledge, will give satisfactory tracings of these very dense spectrograms is the microdensitometer at the McMath-Hulbert Observatory. Through the generous cooperation of Dr. McMath and the staff of the McMath-Hulbert Observatory this instrument was made available to us for our work. All of the results described in this report were obtained from the tracings made at the McMath-Hulbert Observatory.

The spectrograms were traced with a rectangular slit 25μ by 225μ. With this size of slit the grain structure in the film is evident on the tracings, but not to the extent that it requires any appreciable smoothing of the line profiles. A longer slit could not be used because of the large irregularities in the moon's profile. The magnification between the tracings and the spectrograms is 165x. Since the dispersion of the spectrogram is 7.5 A°/mm, the dispersion of the tracings is .045 A/mm or 1.15 A/inch. The slit width corresponds to 0.19 A, and the length of the slit

covers a strip of chromosphere 22,500 km long or about 1.9° of arc on the limb.

Two points on the east limb at second contact were traced on all of the ultraviolet spectrograms. The tracings extend from λ3900 to λ3500. They include the hydrogen Balmer lines from H_8 to H_{∞}, and the Balmer continuum from λ3647 to λ3500. The two points traced are marked "a" and "b" in plate 1. Point a is at a heliographic position angle of 67° and point b at 65°. This region of the sun's limb showed no signs of prominence activity either during the eclipse or during the days immediately following and preceding the eclipse. The red and green coronal lines were at a low intensity at these position angles, but there was a moderate maximum in the green line at 75°, and a weak maximum in the red line also at 75°. However, since these regions were not large, and the main center of the coronal activity had passed the east limb one or two days prior to the eclipse, the chromosphere at these position angles should be representative of the quiet chromosphere. It would be desirable to have tracings at at least one other point on the east limb which is far enough removed from the other points to be independent of any local peculiarities that might be present in the chromosphere at these points. This was not done at the McMath-Hulbert Observatory because the slit in the microdensitometer could not be rotated, and the points near the line of contacts were the only ones where the slit was parallel to the chromospheric crescents.

The relative motion of the moon projected on the sun was 269 kms/sec along the line of contacts. Both of the points considered are so close to the line of contacts that this value can be used without correction. During an exposure that lasted 0.3 second the moon moved 108 km relative to the sun.

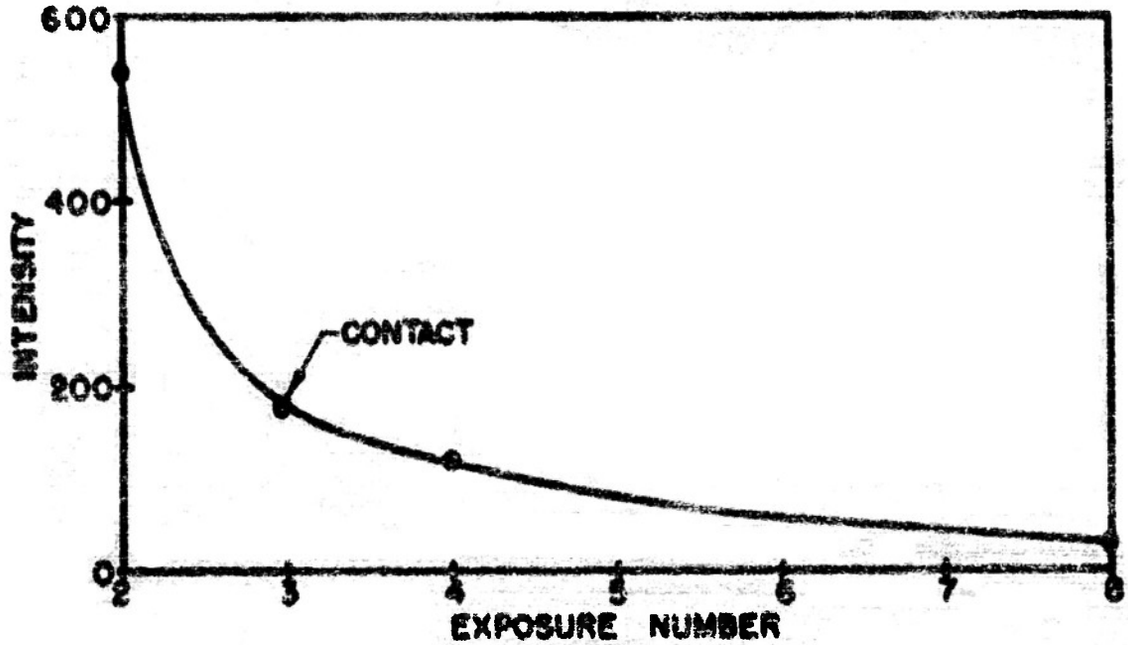

FIG. 7 CONTINUUM INTENSITY

The effective height for each exposure was assumed to be the point reached by the moon's limb at the middle of the exposure. The heights are measured from the photospheric limb, which was determined by plotting the intensity of the continuum at λ3700 for point b against the exposure number as shown in Figure 7. The point at which the slope of the curve changes most rapidly was considered to correspond to the limb of the sun. The point of zero height was selected for point b at exposure number 3.0. This should be within ± 20 km of the true position of the edge of the photosphere. Point a was apparently at contact before any usable exposures were obtained. The moon profile pictures show an effective difference in the average elevation of the two points of about 700 km when projected on the chromosphere. Over the length of the slit the extreme variations in the moon profile project

as about 100 km in the chromosphere. The average variations are much less than this, but they are enough to make the effective difference of the two points uncertain to perhaps ± 75 km.

Another method of determining the difference in height between points a and b is to compare the intensities of the chromospheric lines with large height gradients at the two points. The CN band at λ3883 is convenient for this comparison. The exposures on which the band has the same intensity at the two points are separated by 650 km. A visual inspection of numerous weak lines at the two points also gave an average difference of 650 km. The 650 km value was adopted as the difference in the effective height in the chromosphere for the two points on the same spectrogram. The heights assigned to each spectrogram are listed in Table 2.

The microdensitometer tracings were converted to line intensities in the following fashion. First, the microdensitometer tracings of the spectrograms were calibrated by tracing a step wedge of known densities, which was printed on the same emulsion as the spectrograms. The calibrations were made several times during the tracing of each spectrogram so that convenient sensitivity settings could be used in all regions of the spectrum. The density in a line profile was read every one-sixth of an inch on the tracings, or, in other words, every 0.2 A in the spectrum. The densities were converted to intensities by means of the characteristic curves of the preceding section, and replotted on a larger scale. Line profiles were then drawn as smooth curves through the points, and the areas under the curves measured with a planimeter. The area under the curves gave the value of the line intensities as expressed by equation (9). However these line intensities must still be corrected for variations in exposure time and

those on the secondary spectra must be converted to the scale of the primary spectra by application of the ratio of intensities between the two. The methods for these corrections are described below.

We attempted to smooth a few of the obvious defects in the film, but made no attempt to force the unblended profiles into any sort of a pattern. Except for the obvious defects and blends with other lines the intensities at each point are taken directly from the microdensitometer tracings, and the characteristic curve at that wavelength. The profiles were drawn to give the best smooth fit to these points. In the cases where the Balmer lines were blended with other lines in such a way that the two were not resolved, the intensity given was the sum of the intensities for the two lines. In the Balmer lines H_{26}-H_{31}, and in other Balmer lines that are close to non-Balmer lines, the wings of the lines are overlapped. In order to separate these lines the continuum intensity vs wavelength curve was extrapolated to include the wavelengths of these lines. The lines were then separated by extending the individual profiles of the lines down to the extrapolated continuum in such a way that they have the same shape as the neighboring Balmer lines, and when added together will reproduce the tracing. The blending was not serious enough that the peaks of the lines have been affected, and the line intensities obtained in this way are consistent with the intensities of the rest of the lines in the series. Some of the series lines beyond H_{31} can be identified. We have not made a systematic attempt to identify these lines, but a tentative identification shows that H_{36} is definitely discernible on some spectrograms, and H_{37} is quite probable. All of the series lines beyond H_{31} are too badly affected by blends, and reliable intensities are impossible.

Probable errors in the relative intensities obtained may be estimated by examining each of the five basic steps in the process of their determination. These five steps are the following: (1) photographing the spectrum; (2) measuring the densities on the spectrograms; (3) converting the densities to intensities through the characteristic curves; (4) drawing the intensity profiles; and (5) measuring the areas under the profiles. There are random errors in all of these steps, but, the only likely systematic errors are caused by errors in the characteristic curves. The random errors in the individual steps are hard to evaluate, but, at least in this case, the errors from the last three steps are small compared to those from the first two steps. The most serious random errors are caused by inhomogeneities in the emulsion and other defects in the spectrograms. The total random error introduced by the last four steps can be evaluated by repeating all of the processes several times for a given line, or two or three times for several lines. In making the tracings there were many curves where the same line on a given spectrogram was traced two or three times on different occasions. Of 54 such cases, the maximum difference in the log of the intensity was 0.08, and the probable error was $\pm$ 0.027 in the log of the intensity. Most of this error is in the microdensitometer tracing, and the biggest share of it comes from small differences in the position of the slit on the spectrogram.

Besides the random errors in the spectrograms caused by defects in the emulsion, there are random errors caused by defective shutter action and other instrumental difficulties. The defective shutter action does not cause random errors in the relative intensities at one point on the limb in a given spectrogram. However, when the intensities at two points on the

limb, or at the same point on the limb in different spectrograms, are compared the defective shutter action can cause large errors. Fortunately, these errors can be evaluated and corrected. The clocks in the data panel image were placed there in anticipation of correcting errors from this source. The obscuring of most of these images by the coronal continuum seemed, at first, to present an insurmountable barrier to any attempt to evaluate these errors. Once again, however, the corona had merely substituted something better.

As was pointed out earlier, the image of the corona bordering the dark image in the spectrograms is from a source of constant intensity. The density at a fixed point in this image is, then, a measure of the total exposure at that point. If we assume that the exposure time for this point in the corona has the same ratio to the exposure times at the two points a and b in all spectrograms, then we can use the relative exposure in the image of the corona on each spectrogram to correct all intensities to a standard exposure. There is probably some variation in the ratio of the exposure times at two points at the same wavelength in different spectrograms, but this variation was small compared to the variation in total exposure times. The relative exposures were measured at four points in the image of the corona on all of the spectrograms. In all cases the four points showed the same relative exposure within the accuracy of the density readings. The averages of the four corrections necessary to bring each of the exposures to a standard 0.3 second exposure are listed in Table 8 in the Appendix, and it is these values that we used to correct our computed intensities.

To convert exposures to exposure times, we used Schwarzschild's

reciprocity law[15]

$$E = It^{p} \qquad (18)$$

relating the total exposure, E, to the intensity, I, and the time, t. This law can be used to calculate fairly accurate values for the exposure times. p has been determined by assuming that the 2.9 seconds was the correct exposure time for exposure number 23, and that exposure number 9 was 0.20 second as shown by the clocks in the data panel. The same value of p is used to calculate all of the exposure times. The calculated times are given in column six of Table 8 in the Appendix. The agreement of these times for the six cases where the clocks would be read was very good.

It should be noted that there is no tendency for the correction to the 0.3 second exposures to change systematically with time. A small systematic change would be masked by the scatter in the corrections, but a change of any significance, as would occur if the intensity in the image of the corona was changing significantly, during the eclipse, would be detectable. Exposure number 19 should have been 0.9 second; the clocks in the infrared data panel show an exposure of 0.66 second, and those in the visible show 0.58 second. They also show a complete cycle of 0.7 second, and not 1.0 second as it should have been. This performance quirk is completely unexplained.

In order to relate the intensities of the lines in the secondary to those in the primary images, we must know the ratios of the intensities in the two images. Unfortunately, this ratio was not the same for all exposures because of the irregular operation of the shutters. The ratio can be determined for each spectrogram from the integrated intensities of the lines in the two images. If, for a given spectrogram, the log of the intensities

of the Balmer lines are plotted against the line numbers, the curves obtained from the two images are separated by the log of the intensity ratio. In most cases the two curves have a few lines in common, and there was no difficulty in joining the two curves. The values obtained in this way are entered in the last two columns of Table 8 in the Appendix. In all except three cases the values were within $\pm$ 0.10 of the average value of 2.10. The values for the two points on the limb showed slight differences. Most of this was undoubtedly due to errors in matching the curves. The best way to apply these corrections to the line intensities is somewhat uncertain. The procedure which we followed is to correct all of the secondary image intensities by the average value of 2.10 plus one-half of the residual, and to correct the primary dark image intensities by minus one-half of the residual, or, if all of the lines were measured in the secondary image the average correction was used.

After these corrections were made the log of the intensity of each line was plotted against the height at each point on the limb. There were no apparent differences shown by the data from the two points on the limb. In each case, however, there were obvious irregularities in the intensities on a few of the spectrograms. These irregularities showed up in all the lines on a given spectrogram. In the cases of exposure numbers 8, 9, and 13, the intensities in the primary image were too low and those in the secondary image too high. In the cases of exposures 12 and 14, the reverse was true. This was quite obviously caused by an incorrect application of the correction for the intensity ratio. In all of these cases, if all or most of the residual, rather than simply half of the residual, was used to correct the intensities in the primary image, the data were more consistent,

and in these cases the full residuals have been used to smooth the data. There is further evidence that the residuals were mainly caused by the primary image. If all of the intensities in the secondary images were corrected by the average value of 2.10, the line intensities from the secondary images showed a smooth curve with very little scatter, whereas the intensities in the primary images showed systematic errors similar to the residuals. The cases in which the full residual was used to correct the primary image intensities were the ones which showed the most serious systematic errors.

In order to help reduce the uncertainties caused by the random errors remaining in the data, the intensities from the two points on the limb were combined. This, in effect, doubled the number of observations. It is true, of course, that the random errors were not all independent in this case. The errors which resulted from defective shutter action were very nearly the same at the two points on the limb, but the two points were at considerably different heights in the chromosphere, and when the data were plotted these errors therefore appeared at different heights.

The log of the corrected integrated line intensities in ergs/sec are tabulated in Table 2. The emission was assumed to be uniform in all directions, and was integrated over a slice of chromosphere bounded by two parallel planes 1 cm apart which are in the line of sight and perpendicular to the moon's limb, and a third plane in the line of sight which is tangent to the moon's limb. These data are plotted in Figure 8. The scatter in the data resulted from random errors from all sources, including incorrect application of the correction for the intensity ratio in the two images. The scatter was appreciable, but the observations were numerous enough that

Table 2
Line* and Continuum** Intensities
Point a

Spec. No.	2	3	4	8	9	10	11	12	13	14	15	16	17	18	19	20	21	22
Exp. No.	2	3	4	8	9	10	11	12	13	14	15	16	17	18	19	20	21	22
Height km	630	640	730	1180	1280	1390	1500	1610	1720	1830	1930	2040	2150	2260	2360	2470	2580	2780
Hα	3.44	3.11	3.14	2.79	2.82	2.78	2.80	2.48	2.65	2.63	2.58	2.46	2.44	2.38	2.44	1.78	1.64	
9	3.14	2.91	2.91	2.59	2.64	2.49	2.58	2.47	2.30	2.27	2.20	2.12	1.94	1.92	1.92	1.30	1.08	
10	2.98	2.80	2.81	2.50	2.40	2.41	2.34	2.38	2.23	2.15	2.07	1.99	1.85	1.80	1.78	1.32	0.98	
11	2.89	2.78	2.78	2.41	2.33	2.27	2.26	2.24	2.07	2.02	1.97	1.92	1.78	1.64	1.63	1.00	0.88	
12	2.88	2.69	2.73	2.38	2.29	2.15	2.20	2.13	1.98	1.96	1.91	1.70	1.83	1.66	1.52	0.90	0.89	
13	2.83	2.64	2.70	2.31	2.20	2.15	2.18	2.00	1.97	1.76	1.79	1.68	1.60	1.46	1.48	0.84		
14	2.74	2.61	2.66	2.23	1.98	2.06	1.98	1.95	1.78	1.72	1.61	1.60	1.57	1.45	1.40			
15	2.58	2.49	2.60	2.10	1.97	1.89	1.85	1.96	1.67	1.68	1.56	1.58	1.30	1.15	1.37			
16	2.51	2.37	2.48	2.00	1.96	1.88	1.72	1.78	1.54	1.39	1.50	1.38	1.20	1.09	—			
17	2.45	2.30	2.40	2.02	1.95	1.74	1.65	1.68	1.45	1.38	1.46	1.34	1.04	1.06	1.02			
18	2.36	2.27	2.26	1.96	1.93	1.68	1.55	1.58	1.43	1.31	1.33	1.16	0.94	0.97	0.94			
19	2.26	2.29	2.24	1.87	1.70	1.78	1.50	1.60	1.34	1.32	1.33	1.15	0.95	0.98	0.89			
20	2.26	2.20	2.19	1.78	1.86	1.86	1.53	1.46	1.29	1.33	1.21	0.99	0.88	0.78	0.77			
21	2.20	2.17	2.22	1.84	1.85	1.47	1.61	1.38	1.21	1.20	1.11	0.90	0.75	0.74	0.75			
22	2.15	2.05	2.06	1.90	1.53	1.45	1.34	1.24	1.15	1.18	--	0.84	0.70	0.64	0.61			
23	2.18	2.05	2.01	1.86	1.39	1.38	1.28	1.22	1.08	1.08	0.84	0.78	0.70	0.62	0.68			
24	2.08	1.97	1.95	1.48	1.53	1.19	1.19	1.04	0.99	0.93	0.81	0.69	0.68	0.58	0.60			
25	2.10	1.98	1.92	1.47	1.38	1.14	1.09	0.96	0.98	0.77	0.76	0.65	0.66	0.56	0.59			
26	1.93	1.89	1.78	1.40	1.34	1.18	1.03	0.94	0.87	0.73	0.72	0.69	0.52	0.38	0.38			
27	1.98	1.84	1.89	1.20	1.10	1.08	0.88	0.86	0.78	0.64	0.65	0.58	0.38	0.38	0.83			
28	2.01	1.86	1.81	1.17	1.17	1.00	0.91	0.88	0.80	0.63	0.60	0.45	0.42	0.80	0.56			
29	1.78	1.73	1.67	1.16	0.98	0.88	0.81	0.68	0.78	0.66	0.49	0.38	0.39	0.51	0.80			
30	2.14	1.96	1.88	1.22	1.23	0.91	0.88	0.79	0.78	0.58	0.60	0.45	0.36	0.35	0.87			
31	1.89	1.68	1.54	0.93	0.84	0.66	0.63	0.89	0.60	0.56	0.39	0.26	0.22	--	0.14			
λ3900**				1.48	1.39	1.40	1.43	1.07	1.31	1.39	1.36	1.31	1.31	1.54	1.15			
λ3640**				1.80	1.69	1.71	1.71	1.66	1.86	1.89	1.87	1.68	1.45	1.42	1.83			
λ3600**				1.78	1.67	1.70	1.70	1.56	1.87	1.81	1.86	1.69	1.44	1.44	1.86			
λ3580**				1.77	1.60	1.66	1.71	1.62	1.88	1.87	1.83	1.68	1.39	1.41	--			
λ3500**				1.78	1.63	1.67	1.68	1.69	1.46	1.86	1.86	1.63	--	1.80	--			
λ3640+	2.43	2.44	2.37	1.83	1.61	1.64	1.61	1.63	1.63	1.19	1.18	1.03	0.87	0.80	0.84			
λ3600+	2.40	2.29	2.48	1.80	1.38	1.63	1.40	1.48	1.86	1.38	1.17	1.07	0.98	0.88	0.70			
λ2800+	2.40	2.06	2.36	1.80	1.36	1.61	1.44	1.40	1.18	1.19	1.13	1.00	0.81	0.78	—			
λ3600+	2.31	—	2.24	1.83	--	1.61	1.40	1.36	1.06	1.19	1.30	0.98	—	0.71	--			

Table 3 (Cont.)

Point b

Spec. No.	4	6	7	8	9	10	11	12	13	14	15	16	17	18	20
Exp. No.	4	8	9	10	11	12	13	14	15	16	17	18	19	23	24
Height km	100	530	640	760	860	960	1070	1180	1280	1380	1500	1610	1750	3590	5060
8	3.87	3.10	3.08	3.10	3.06	3.03	3.00	2.86	2.68	—	2.81	2.79	—	2.01	1.74
9	—	3.06	2.84	2.81	2.80	2.75	2.72	2.65	2.63	2.56	2.53	2.45	2.20	1.70	1.38
10	3.04	2.82	2.74	2.69	2.69	2.63	2.59	2.49	2.48	2.38	2.32	2.31	2.01	1.55	1.24
11	2.99	2.75	2.67	2.60	2.60	2.55	2.51	2.39	2.36	2.26	2.27	2.19	1.93	1.49	1.18
12	2.97	2.76	2.67	2.60	2.59	2.51	2.46	2.36	2.36	2.28	2.15	2.13	1.88	1.38	0.97
13	2.98	2.75	2.63	2.56	2.54	2.48	2.46	2.31	2.24	2.09	2.06	2.06	1.73	1.35	0.89
14	2.86	2.68	2.55	2.55	2.45	2.41	2.34	2.21	2.12	2.06	1.93	1.99	1.67	1.30	—
15	2.69	2.62	2.40	2.35	2.29	2.25	2.18	2.06	2.01	1.93	1.88	1.84	1.58	1.10	—
16	2.64	2.48	2.30	2.30	2.20	2.22	2.06	1.97	1.98	1.84	1.87	1.75	1.52	1.07	
17	2.59	2.37	2.26	2.21	2.17	2.13	2.03	1.90	1.84	1.77	1.68	1.68	1.49	0.92	
18	2.43	2.38	2.17	2.14	2.07	2.01	1.93	1.87	1.79	1.65	1.74	1.68	1.41	0.79	
19	2.40	2.27	2.12	2.14	2.11	1.98	1.92	1.81	1.77	1.66	1.63	—	1.29	0.68	
20	2.48	2.28	2.14	2.07	2.01	1.90	1.78	1.74	1.72	1.62	1.65	1.54	1.18		
21	2.37	2.25	—	2.07	2.01	1.77	1.75	1.66	1.66	1.55	1.48	1.39	1.08		
22	2.36	2.08	2.00	1.98	1.91	1.68	1.68	1.60	1.67	1.50	1.30	1.28	1.07		
23	2.27	2.03	1.92	1.87	1.80	1.59	1.57	1.49	1.48	1.36	1.25	1.12	1.02		
24	2.25	1.99	1.88	1.82	1.78	1.56	1.51	1.43	1.30	1.26	1.19	1.04	0.90		
25	2.26	2.01	1.79	1.80	1.75	1.46	1.47	1.38	1.39	1.25	1.11	0.98	0.89		
26	—	1.86	1.75	1.73	1.69	1.39	1.39	1.26	1.27	1.17	1.03	0.93	0.84		
27	2.18	1.79	1.72	1.64	1.65	1.43	1.36	1.23	1.20	1.11	1.08	0.85	0.79		
28	2.29	1.66	1.78	1.60	1.71	1.34	1.30	1.16	1.16	1.08	0.91	0.80	0.72		
29	—	1.68	1.62	1.54	1.54	1.18	1.25	1.09	1.01	0.87	0.68	0.77	0.74		
30	—	1.97	1.81	1.75	1.71	1.32	1.36	1.12	1.19	1.05	0.77	0.64	0.72		
31	—	1.53	1.58	1.43	—	1.07	1.14	0.94	0.81	0.80	0.65	0.59	0.69		
λ3700**				1.87	1.80	1.80	1.45	1.45	1.48	1.39	1.41	1.48	1.84		
λ3640**				2.29	2.41	2.16	1.90	1.98	1.86	1 .	1.78	1.68	1.51		
λ3600**				2.14	2.32	2.12	1.85	1.91	1.85	1.70	1.73	1.70	1.54		
λ3560**				2.05	2.33	2.06	1.80	1.84	1.79	1.62	1.70	1.68	1.57		
λ3500**				2.04	2.07	1.97	1.83	1.81	1.76	1.66	1.69	1.65	1.58		
λ3640*	2.73	2.39	2.32	2.20	2.08	2.06	1.72	1.75	1.66	1.48	1.45	1.36	1.08		
λ3600*	2.74	2.36	2.37	2.01	2.24	2.01	1.85	1.74	1.56	1.44	1.47	1.41	1.15		
λ3560*	2.80	—	2.06	1.92	2.25	1.94	1.56	1.54	1.44	1.31	1.43	1.35	1.22		
λ3500*	2.80	2.31	—	1.80	1.92	1.82	1.64	1.61	1.51	1.40	1.48	1.36	1.19		

* Add 12.00 to all line intensities to get $\log_{10}$ of the integrated emission in the line in ergs/sec from a slice of chromosphere bounded by two parallel planes 1 cm apart which lie in the line of sight, and are perpendicular to the sun's limb; and a third plane tangent to the moon's limb along the line of sight. The emission is assumed to be isotropic.

** These continuum intensities are $\log_{10}$ of the total intensity in the continuum from all sources in ergs/sec/unit frequency.

* These continuum intensities are $\log_{10}$ of the free-bound emission in the Balmer continuums (See text for derivation).

All values below the solid line are measured in the primary image; those above the line are measured in the secondary image.

there are no significant uncertainties in the curves. None of the corrections used, except those for the long exposure times of exposures 19, 22, and 23, altered the shapes of the curves. Indeed, when the data were plotted without corrections at all they still clearly define the same curves that are shown in Figure 8.

The intensities at four wavelengths in the Balmer continuum and outside the Balmer continuum at λ3700 are also included in Table 2. We have tabulated both the total observed continuum intensity from all sources, and the total intensities minus the intensity at λ3700, corrected empirically for the changes in the non-Balmer continuum with wavelength. The variation of this non-Balmer continuum with wavelength was determined from the image of the coronal continuum bordering the primary image of the spectrum.

The log emission vs. height curves of which samples are given in Figure 8 were drawn to give an empirical fit to the data. In all cases except H_{31}, H_{30}, and H_{29} the data are fit by straight lines in the higher levels, but in the lower levels the curves flatten out. The discrepancies in H_{31}, H_{30}, and H_{29} are probably caused by the blend of H_{30} with Ti II. The large gradient of H_{30} in the low chromosphere confirms the results of Cillié and Menzel[2], that the ionized metals have larger height gradients than hydrogen. This same effect is reflected in the two neighboring lines by the overlapping wings of H_{30}. H_8 is blended with He I and seems to exhibit a height gradient a little smaller than would be expected from the gradients of the neighboring lines. This is also consistent with the lower height gradients for He found by Cillié and Menzel. In addition to these blends, H_{28}, H_{19}, H_{14}, H_{13}, and H_{12} all show the effects of blending with neutral and ionized metal lines. These effects show up strongly if the Balmer decrements* read

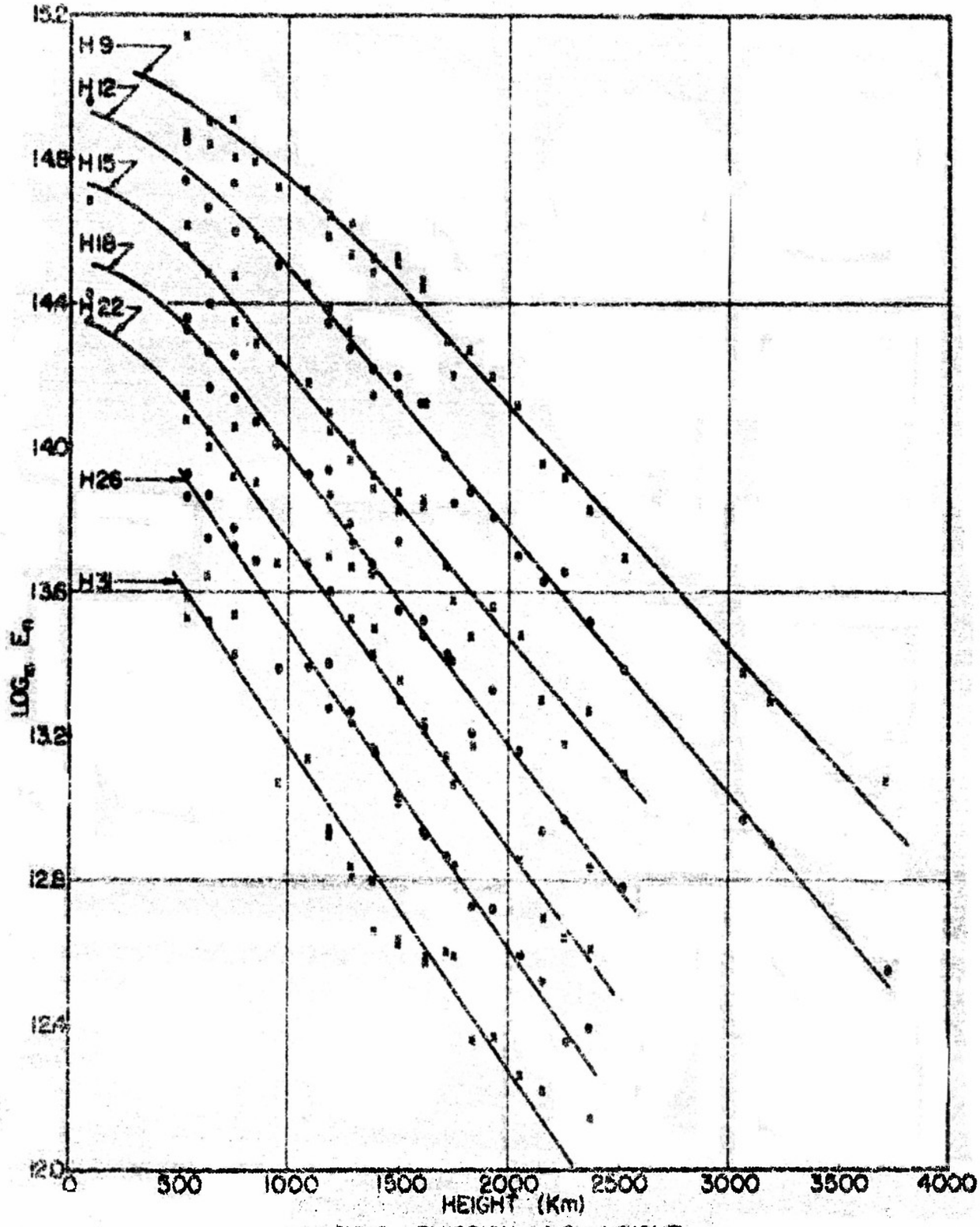

FIG 8 EMISSION VS. HEIGHT

from the curves in Figure 8 are plotted at different levels in the low chromosphere. The Balmer decrements from the data in Table 2 also show these effects, but they are harder to recognize because of the random errors in the data.

The log emission vs. height curves show a systematic decrease in slope from the higher order to lower order lines. This decrease in slope is too large to be due to random errors in the data, and, as will be shown in part V, it is very unlikely that it is due to systematic errors in the photometry. This difference in the slopes means that the Balmer decrement is increasing with height. There seems to be no tendency for the height gradients to approach a common value. In fact, all of the lines seem to reach their maximum slope at fairly low levels in the chromosphere. This point will be discussed further in part VI.

---

* The Balmer decrement is defined as $\log \mathcal{E}_n/\mathcal{E}_{n'}$ where n is the principal quantum number of the upper level of the transition.

V. COMPARISON ON INTENSITIES WITH PREVIOUS OBSERVATIONS

The Balmer decrements have been measured at previous eclipses by Cillié and Mensel[2], Thackeray,[16] and Kiess and Humphreys[17]. These observations have all given consistent results. The most complete and most reliable data are those of Cillié and Mensel. A comparison of our Balmer decrements with theirs is shown in Table 3. The results of Kiess and Humphreys are listed in the last column of Table 3, but the height to which they apply is unknown. For the particular set of lines chosen, the results are all quite consistent. In general, our data show a larger Balmer decrement in the higher levels. Above 1500 km, however, the previous observations are quite sparse and no adequate comparison can be made. Cillié and Mensel's data show unmistakably that the Balmer decrement is increasing with height, but not quite as fast as it is in our data.

Over a restricted range in height, h, we express the observed emission in the Balmer lines as

$$\mathcal{E}_n = \mathcal{E}_{n,0}\, e^{-\beta_n h} \tag{19}$$

where $\mathcal{E}_n$ and β_n are generally different for each line. It follows that

$$\beta_n = -2.303\, \frac{\Delta \log \mathcal{E}_n}{\Delta h} \tag{20}$$

and β_n can be readily obtained from the curves in Figure 8. The values of β_n at two heights in the chromosphere are tabulated in Table 3 along with the values obtained by Cillie and Mensel. The differences between the 1932 data and our data are quite large. These differences, however, are differences in the natural logarithms and should be divided by 2.3 for

comparison. Gillis and Mensel's results are obtained from two intensities that have differences in log E_n of about 0.5. Over the same range in heights our $\Delta \log E_n$ is about 0.7. This is the same direction as the differences we have found in the Balmer decrements, but the percentage difference is much larger. Therefore, it seems unlikely that the differences are entirely due to photometry, and there must be some real differences in chromospheric structure. However, part of the differences observed could be due to photometric errors in either set of data.

The photometry of the 1932 data is based on a system somewhat comparable to our standard exposure. However, in the 1932 data no corrections were made for changes in the characteristic curves with wavelength in the range λλ 4900-3100. The authors point out that any errors arising from this neglect would show up as systematic differences with wavelength of the values of β for the metal lines. No such tendencies were noted, and it was concluded that the neglect was not serious. Since their results include many lines in which such a change could be detected, it is unlikely that there are any large errors from this source. On the other hand, it is also unlikely that the curves would have exactly the same shape over such a wide wavelength range.[18] This, of course, is a property of the emulsion and depends upon the particular film. In fact, the differences between the 1952 and 1932 results are such that it would be difficult, if not impossible, to correct them with any simple distortion of a characteristic curve, and therefore the observed differences more likely represent real differences in the thermodynamic structure of the chromosphere at the two times.

Although we cannot prove conclusively that our characteristic curves

Table 3

Balmer Decrements

$H_n - H_{n+k}$	log $K_0/K_n + k$ 670 km 1932	1952	1500 km 1932	1952	2330 km 1932	1952	3170 km 1932	1952	† 1940
8 - 12	0.40	0.41	—	0.67	—	0.77	0.81	0.85	0.41
12 - 15	0.22	0.25	0.25	0.28	0.26	0.30	—	—	0.21
15 - 18	0.20	0.22	0.16	0.26	—	0.31	—	—	0.22
18 - 21	0.10	0.10	0.18	0.15	—	0.21	—	—	0.12
21 - 24	0.19	0.22	0.27	0.25	—	0.27	—	—	—
24 - 27	0.11	0.18	0.10	0.18	—	0.19	—	—	—
27 - 31	0.15	0.23	—	0.25	—	0.26	—	—	—

Table 4

β_n

H_n	$\beta_n \times 10^8 cm^{-1}$ 1000km 1952	2000km 1952	1932	H_n	$\beta_n \times 10^8 cm^{-1}$ 2000km 1952	1932
H_8	0.93	1.39	1.20	H_{20}	1.91	1.39
H_9	1.16	1.51	1.22	H_{21}	1.96	1.42
H_{10}	1.39	1.56	1.22	H_{22}	1.96	1.33
H_{11}	1.45	1.62	1.22	H_{23}	1.96	1.47
H_{12}	1.68	1.68	1.22	H_{24}	2.05	1.47
H_{13}	1.68	1.68	1.25	H_{25}	2.08	1.58
H_{14}	1.70	1.70	1.25	H_{26}	2.05	1.64
H_{15}	1.73	1.73	1.30	H_{27}	2.08	1.61
H_{16}	1.73	1.73	1.36	H_{28}	2.12	1.50
H_{17}	1.79	1.79	1.28	H_{29}	2.08	1.52
H_{18}	1.85	1.85	1.20	H_{30}	2.12	1.54
H_{19}	1.91	1.91	1.30	H_{31}	2.12	1.54

are free from systematic errors, there is considerable evidence in their favor. Some of this evidence has been discussed in part IV. We showed that the method of constructing the curves, as described there, gave curves that were internally consistent. Our confidence in them was bolstered by the consistency of the extreme ends of the curves, which were checked by means of the relative intensities of several lines in the two images of each spectrum. Moreover, from this we obtained an intensity ratio between the primary and secondary images for selected exposures and the ratios so obtained were in very good agreement with the ratios obtained independently from the integrated line intensities on the same spectrograms. This is a rigorous check on the internal consistency of the curves, though not necessarily a check on the shapes of the curves. The Boulder standard exposures show disagreement with these curves in the regions where the Boulder curves are known to be in error, and good agreement throughout the straight line portions and high density ends of the curves where they are more likely to be correct. This is perhaps not a clear demonstration of accuracy, but it at least strongly corroborates the curves.

There is one other consideration that shows both consistency and accuracy in our curves. The intensities of the lower order lines H_8-H_{15} were measured in all cases in the secondary images. In the early exposures the line densities lay in all parts of the curve except the toe. In the later exposures the densities lay lower in the curve, in the straight line portions of the curve and all parts of the toe save the extreme end. On the other hand, in the higher order lines, say H_{20}-H_{31}, the intensities were measured in the secondary images in the low chromosphere and in the primary images in the higher chromosphere. The result is that in the

early exposures the densities in these higher order lines were near the toe of the curve, but as soon as the densities became too weak for accurate photometry, the line intensity was measured from the primary image, giving densities up above the straight line portion of the curve. On still later exposures the densities in these lines dropped down to the straight line portion of the curve again.

In spite of this jumping around on the characteristic curve the data were very consistent, as evidenced by the height gradient curves. If the curves were seriously in error there would be abrupt discontinuities in these height gradients corresponding to each change of range on the curve. Therefore we conclude that photometric errors in our data are not likely to be the cause of the differences between the Khartoum eclipse results and those of 1932.

Further evidence for real differences in the chromospheric structure at the two eclipses is given by the absolute intensities and the maximum heights to which the lines were observed. In the low chromosphere our absolute intensities are of the order of 0.6 to 0.7 in $\log_{10}$ higher than the intensities in the 1932 data. This is probably a real difference as shown by the fact that in our data the higher order lines are observable to higher levels than in 1932 even though the height gradients are larger. It should be recognized, of course, that this may be a result of the greater speed of our spectrographs and consequently greater exposure in our spectrograms. On the other hand, a really brighter chromosphere may be the reason that our spectrograms were somewhat overexposed; the exposure times were computed on the basis of intensities given in the 1932 data.

If we compare the estimated maximum heights of the Balmer lines for

the 1952 eclipse with those reported by Wildt[19] for four previous eclipses, we find that we have observed H_{31} to some 1000 km higher than in the previous cases. For the lower order lines, this difference gradually decreases until at H_{16} the maximum heights seem to be about the same (see Table 5). This is consistent with the fact that the height gradients and absolute intensities were larger in our eclipse data. Mitchell[20] has reported similar differences in visual estimates of relative intensities and height gradients in previous eclipses, and Cillié and Mensel have reported large differences from point to point at the same eclipse. These results strongly suggest that both the height gradients and the absolute intensities in the chromosphere were greater during the 1952 eclipse than they were during the 1932 eclipse. Both eclipses were near minimum phase in the sunspot cycle, so that gradual changes with phase of the sunspot cycle cannot be sought as an explanation of our observations.

Table 5

Maximum Heights (km) of Lines

H_n	1952	1905/25	1930/37
H_9	-	7000	7000
H_{16}	3700	4000	4000
H_{20}	3150	2500	2500
H_{23}	2900	2000	2000
H_{26}	2600	1800	1800
H_{31}	2400	1000	1000

VI. PRELIMINARY INTERPRETATION OF DATA

The objective of the work described in this section was to obtain a preliminary idea of the thermodynamic structure of the chromosphere indicated by the Balmer line and continuum data derived and tabulated in the preceding sections. Specifically, we made preliminary determinations of the following: (1) kinetic temperature gradients with height; (2) electron density gradients with height; (3) self absorption for H_γ as a function of height; and (4) departures from thermodynamic equilibrium as a function of height.

The results given here are of the nature of most preliminary estimates of the quantities described. Systematic and careful treatment of the full potentialities of the data is being conducted this summer at the High Altitude Observatory by Dr. Richard N. Thomas, and a group of assistants, including the writer

The general equations for the observed emission in chromospheric lines or the continuum of the Balmer spectrum are first derived. The intensities in slitless spectrograms as tabulated in Table 2 refer to the emission integrated both along the line of sight and from the moon's limb outward. If $\varepsilon_n/4\pi$ is the emission in ergs/sec/cm^{-3}/unit solid angle in the line H_n that escapes the chromosphere in the direction, y, towards the observer, then the emission per unit solid angle in the line from a 1 cm wide slice is

$$\frac{E_n}{4\pi} = \int_h^\infty \int_{-\infty}^{\infty} \frac{\varepsilon_n}{4\pi}\, dy\, dx \qquad (21)$$

where h is the height of the moon's limb above the sun's limb. The geometrical situation is represented in Figure 9. The notation used by

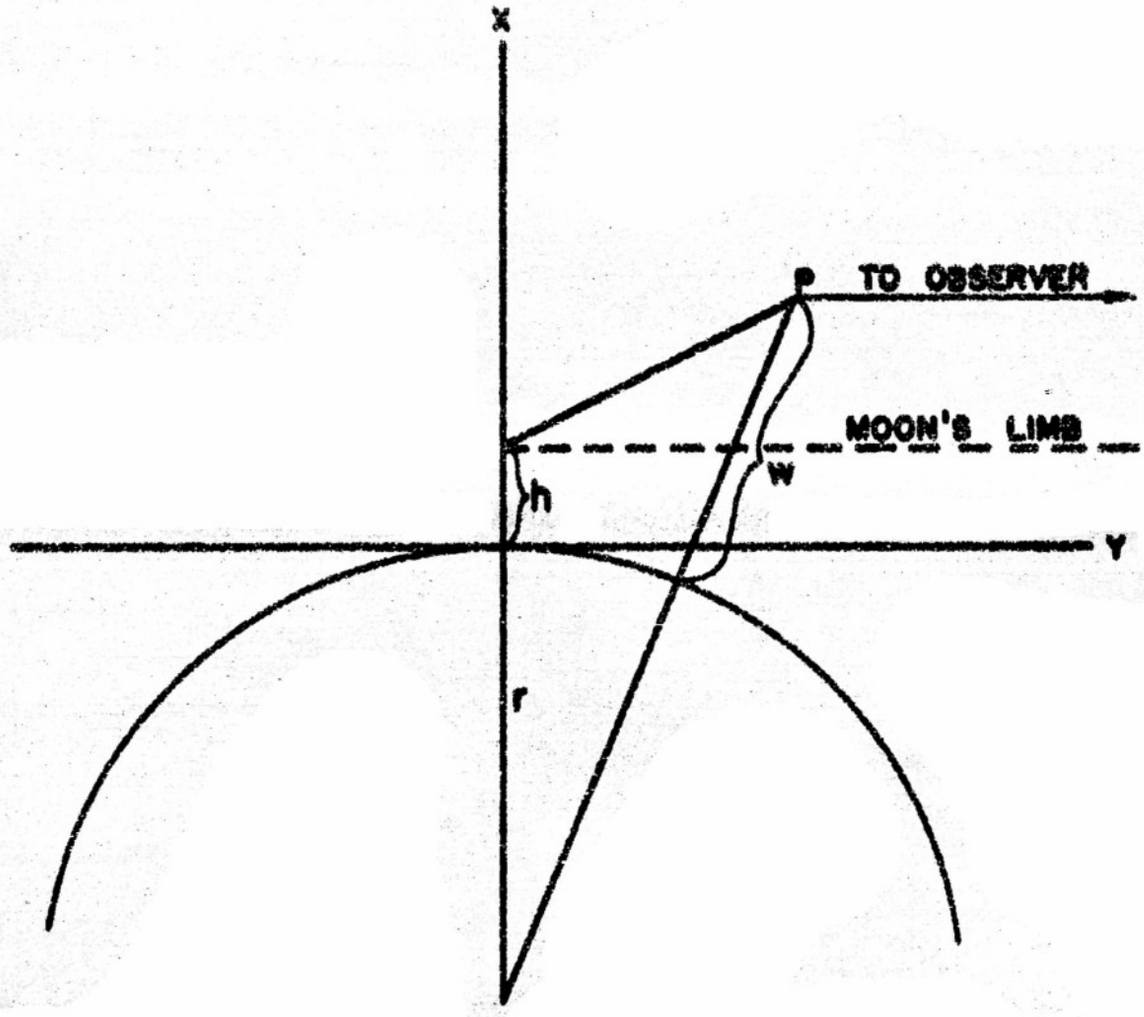

FIG. 9 GEOMETRICAL SITUATION

Thomas[21] has been adopted here to avoid unnecessary confusion. In the chromosphere $\omega \approx \chi$, and to a good approximation

$$\omega = \chi + \frac{\gamma^2}{2\pi} . \tag{22}$$

Let:

ν_n = the frequency of the Balmer line originating from the nth level.

$A_{n,2}$ = the Einstein transition probability for spontaneous transitions from the level n to the level 2.

N_p, N_e = the number of protons and electrons per cm^3.

T_e = the kinetic temperature of the electrons.

ϖ_n = the statistical weight of the level n.

N_n = the number of atoms per cm^3 excited to the level n.

Then for an optically thin atmosphere in thermodynamic equilibrium, denoted by the asterisks, we have a definition of the $A_{n,2}$

$$\mathcal{E}_n^* = h\nu_n A_{n,2} N_n^* \tag{23}$$

where N_n^* is given by the Boltzmann-Saha equation

$$N_n^* = N_p N_e \left(\frac{h^2}{2\pi m k T_e}\right)^{3/2} \frac{\varpi_n}{2} e^{hRc/n^2 k T_e} \tag{24}$$

In general some of the radiation will be reabsorbed. If we call the absorption coefficient $\alpha_{n,2}$ the amount of radiation escaping the atmosphere is

$$\mathcal{E}_n = \mathcal{E}_n^* e^{-\alpha_{n,2} \int_x^\infty N_2(x,y)\, dy}$$

where u is the value of y at the emitting element. Since the chromosphere is predominantly hydrogen, we take $N_p = N_e$. If, in addition, we allow for departures from thermodynamic equilibrium and define b_n by

$$b_n = \frac{N_n}{N_n^*} \tag{25}$$

where N_n is the actual population of the level n and N_n^* is the population of the level in the case of thermodynamic equilibrium, we get for the actual emission which escapes the chromosphere

$$\mathcal{E}_n = h\nu_n A_{n,1} \frac{\Phi_{\nu_n}}{2} \left(\frac{h^2}{2\pi m k}\right)^{3/2} b_n N_e^2 T_e^{-3/2} e^{hRC/\lambda_0 k T_e} e^{-\alpha_{n,1}\int_u^\infty \kappa_\nu \, dy} \tag{26}$$

For convenience, let

$$\chi_n = \frac{hRC}{\lambda^2 k T_e} , \tag{27}$$

$$K = h\left(\frac{h^2}{2\pi m k}\right)^{3/2} \tag{28}$$

and

$$C_n = \nu_n A_{n,1} \frac{\Phi_{\nu_n}}{2} . \tag{29}$$

Equation (26) then becomes

$$\mathcal{E}_n = K C_n b_n N_e^2 T_e^{-3/2} e^{\chi_n} e^{-\alpha_{n,1}\int_u^\infty \kappa_\nu(x,y)\, dy} , \tag{30}$$

and equation (21), multiplied by $h\Pi$, becomes

$$E_\eta = K C_n \int_\lambda \int_{-\infty}^{\infty} b_n N_e^2 T_e^{-3/2} e^{\chi_n} e^{-\alpha_{n,1}\int_u^\infty \kappa_\nu(x,y)\, dy} dy\, d\nu . \tag{31}$$

Menzel[22] has shown that the intensity in ergs/sec/cm^3/unit frequency in the Balmer continuum can be expressed in a similar fashion. For the intensity at wavelength λ in the continuum, he gives

$$\mathcal{E}_\lambda = 2.63 \times 10^{-33} N_e^2 T_e^{-3/2} e^{\chi_\lambda} . \qquad (32)$$

Hence, the observed emission is

$$E_\lambda = 2.63 \times 10^{-33} \int_\lambda \int_{-\infty}^{\infty} N_e^2 T_e^{-3/2} e^{\chi_\lambda} \, dy \, d\tau . \qquad (33)$$

To be strictly correct we should include a b_λ and an absorption term in equation (33). However, both of these are negligibly small in the continuum.

A. Preliminary Analysis of the Balmer Continuum Data

Since the Balmer continuum emission is relatively free from the effects of self-absorption, one can readily obtain estimates of electron temperature and density from the continuum intensities. For the method followed here, it is necessary that the values of $\mathcal{E}_\lambda$ that are used represent only the free-bound emission in the Balmer continuum. The continuum intensity at a point in the slitless spectrograms on the long wavelength side of the Balmer series limit is the sum of the continuum intensities from the various sources integrated over a 1 cm slice of chromosphere and corona. The largest part of this intensity comes from scattering of photospheric radiation by free electrons. On the short wavelength side of the Balmer series limit, the intensity of the free-bound emission in the Balmer continuum is added to the other sources.

Since the exposures in the primary image were quite heavy, we were able to get reliable measurements of the total intensity in the continuum

both on the long wavelength and short wavelength sides of the Balmer series limit. If one knows the relative intensity in the non-Balmer continuum as a function of wavelength, then from the intensity at, say, λ3700 the non-Balmer continuum intensity at shorter wavelengths can be obtained by extrapolation. It is apparent from the spectrograms that a large percentage of the total continuum intensity is coming from the corona. The intensity distribution in this part of the continuum can be determined from the image of the corona bordering the primary image of the spectrum. The largest part of the remaining intensity on the long wavelength side of the Balmer continuum is from scattering by free electrons in the chromosphere, which at low heights is a very substantial contribution. Thus, the intensity distribution in this part of the continuum should be the same as that in the coronal continuum, and the intensity distribution in the total continuum intensity should be very nearly the same except for the perturbation caused by the Balmer continuum.

The intensity distribution in the coronal continuum was measured on several spectrograms. The individual values show considerable variations apparently caused by scattered light in the spectrographs. The average values and the probable errors are shown in Table 6.

Table 6

Relative Intensities in the Coronal Continuum

λ	$\log\left(E_\lambda / E_{3700}\right)$
3900	+ 0.01 ± 0.02
3800	+ 0.00 ± 0.02
3700	0.00
3600	- 0.01 ± 0.02
3500	- 0.03 ± 0.02

At points a and b on the limb the total intensities at λ3700 and at four wavelengths in the Balmer continuum were measured and entered in Table 2. The intensity at λ3700 was then extrapolated to shorter wavelengths by applying the corrections shown in Table 6. This extrapolated intensity was then subtracted from the total intensity at the same wavelength. The remainder was considered to represent the free-bound emission in the Balmer continuum, and these values were entered in the last four rows of Table 2. These data represent the observed emission as expressed by equation (33).

As a first approximation, the graphs of log E_λ vs. height were fitted by straight lines though, as shown below, this leads to unacceptable results. A least squares fit gave the following equations:

$$\log E_{3640} = 2.89 \pm 0.04 - (0.95 \pm 0.03) \times 10^{-8} h . \qquad (34a)$$

$$\log E_{3600} = 2.83 \pm 0.04 - (0.91 \pm 0.03) \times 10^{-8} h . \qquad (34b)$$

$$\log E_{3550} = 2.79 \pm 0.04 - (0.91 \pm 0.03) \times 10^{-8} h . \qquad (34c)$$

$$\log E_{3500} = 2.73 \pm 0.04 - (0.89 \pm 0.03) \times 10^{-8} h . \qquad (34d)$$

The fit of equation (34a) to the observed values of log E_{3640} is shown in Figure 10. For the case of an exponential change of emission with height, we have

$$E_\lambda = E_{\lambda,0}\, e^{-\beta_\lambda h} , \qquad (35)$$

and it follows from (21) that

$$\varepsilon_\lambda = \frac{\beta_\lambda^{3/2}}{(2\pi\kappa)^{1/2}} E_\lambda . \qquad (36)$$

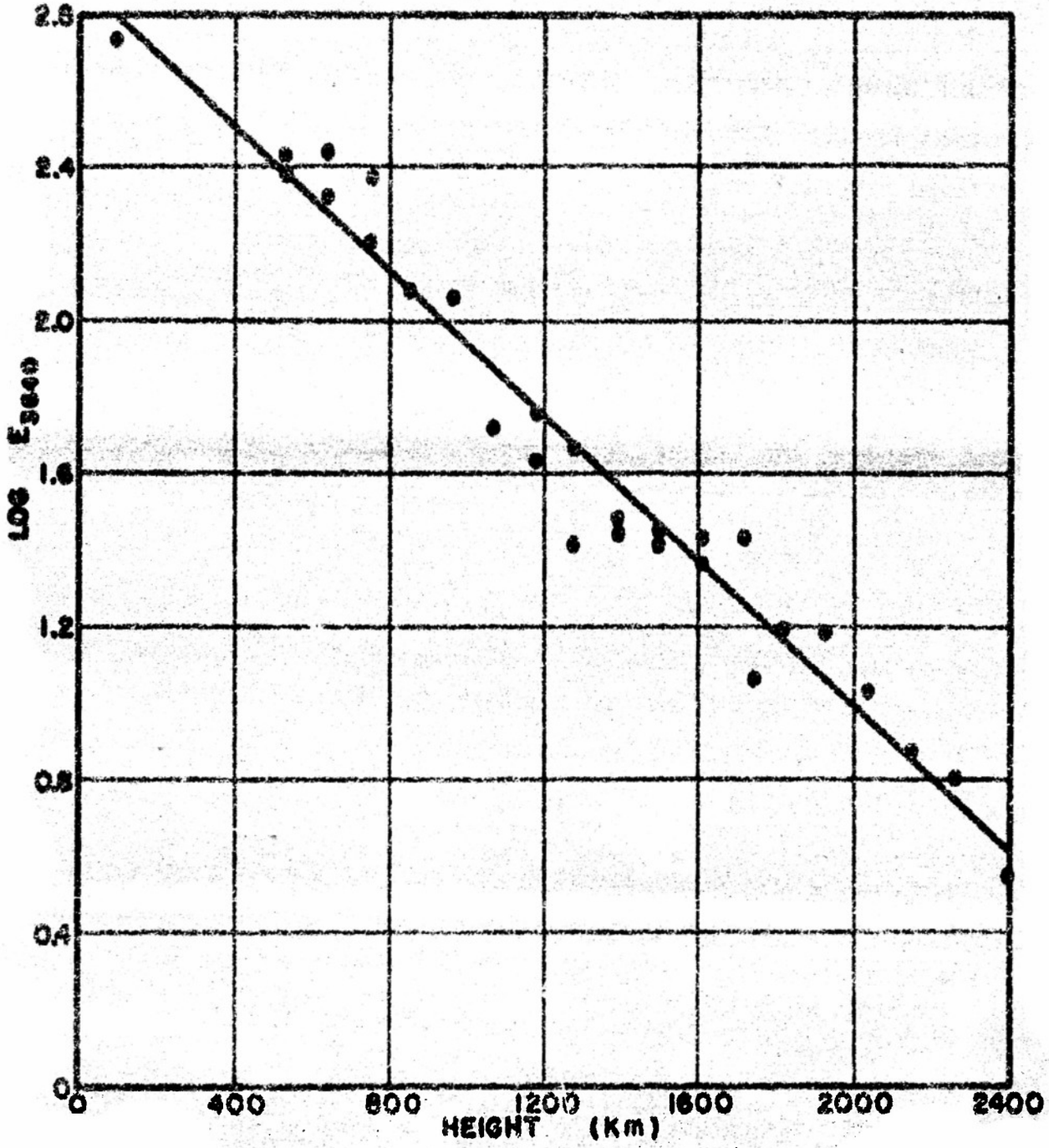

FIG. 10 LOG E_{3640} VS. HEIGHT

Hence the equations (34) can be written as follows:

$$\ln \varepsilon_{3640} = -33.20 \pm 0.09 - (2.19 \pm 0.07) \times 10^{-8} h \,. \tag{37a}$$

$$\ln \varepsilon_{3600} = -33.41 \pm 0.09 - (2.10 \pm 0.07) \times 10^{-8} h \,. \tag{37b}$$

$$\ln \varepsilon_{3550} = -33.50 \pm 0.09 - (2.10 \pm 0.07) \times 10^{-8} h \,. \tag{37c}$$

$$\ln \varepsilon_{3500} = -33.66 \pm 0.09 - (2.05 \pm 0.67) \times 10^{-8} h \,. \tag{37d}$$

From equation (32), we get

$$\ln \varepsilon_\lambda = -25.00 + 2 \ln M - \tfrac{1}{2} \ln T_e + \chi_\lambda \,, \tag{38}$$

$$\frac{\partial \ln \varepsilon_\lambda}{\partial \lambda} = \frac{hc}{k T_e \lambda^2} \,, \tag{39}$$

$$\frac{\partial^2 \ln \varepsilon_\lambda}{\partial \lambda \, \partial h} = -\frac{hc}{k T_e \lambda^2} \frac{\partial \ln T_e}{\partial h} \tag{40}$$

and

$$\frac{\partial \ln \varepsilon_\lambda}{\partial \lambda} = 2 \frac{\partial \ln M}{\partial h} - \left(\tfrac{1}{2} + \chi_\lambda \right) \frac{\partial \ln T_e}{\partial h} \,. \tag{41}$$

Since T_e cannot depend on the wavelength at which we measure it, and since the left side of (40) is independent of height, the consequence of using straight lines to fit the data in the Balmer continuum is that we must have

$$\frac{1}{T_e} \frac{\partial \ln T_e}{\partial h} = \text{const.} \tag{42}$$

The use of straight lines also requires that, unless $\frac{\partial \ln T_e}{\partial h} = 0$, we must have $T_e = \infty$ at some finite height where the lines intersect. In this case the lines at λ3640 and λ3500 intersect at about 2700 km. This is, of course, an unacceptable result, and we should look for departures from

straight lines in the log E_λ vs. height curves.

An alternative approach, not used, would be to consider the observed values of $\frac{d \ln C_\lambda}{d \lambda}$ at each height and obtain T_e at each height from these values. Before this approach could be carried out, however, it would be necessary to refine the measurements in the Balmer continuum. The existing data have so much random error that when individual levels are considered the values of T_e range from a few thousand degrees to ∞. The values of ∞ are obtained both in the higher and lower levels of the chromosphere, and it is impossible to get an average temperature.

Still another alternative for analysing the continuum data was proposed independently by Thomas[7] and Zanstra.[23] This method shows promise of giving much more reliable values for the electron temperature because it is not as sensitive to small errors in the data.

At the present time we are carrying out more extensive measurements of the continuum intensities as a function of wavelength from λ3900 to λ3400, but these results are not yet available. The random errors are being reduced as much as possible by using several measurements of the intensity at each wavelength on each spectrogram. When these measurements are completed we will carry out the analysis proposed by Thomas[7] and further analysis of the intensity distribution within the free-bound emission from the Balmer continuum.

As a preliminary measure, we found it interesting to see what sort of values of T_e, $\frac{d \ln T_e}{d h}$, N_e, and $\frac{d \ln N_e}{d h}$ we could get from equations (37) to (41). These values are tabulated in Table 7. The values of $\frac{d \ln N_e}{d h}$ were obtained by setting $\chi_\lambda = 0$ at λ3640, thus giving

$$\frac{\partial \ln \varepsilon_{3640}}{\partial h} = 2\,\frac{\partial \ln N_e}{\partial h} - \frac{3}{2}\,\frac{\partial \ln T_e}{\partial h} \qquad (43)$$

from equation (41).

It should be noted that the probable errors in equations (37) are of the same order as the differences from which we calculated T_e and $\frac{\partial \ln T_e}{\partial h}$. In fact, if we include probable errors, we get at 1000 km

$$3300^\circ K < T_e < 10,000^\circ K$$

and

$$0.2 \times 10^{-11}\,cm^{-1} < \frac{1}{T_e}\,\frac{\partial \ln T_e}{\partial h} < 1.5 \times 10^{-11}\,cm^{-1}.$$

Hence, the values of T_e and $\frac{\partial \ln T_e}{\partial h}$ in Table 7 can be in error by rather large amounts. Nevertheless, it is unlikely that the data could be in error enough to give $T_e > 12,000^\circ$ K in the low chromosphere. For example, at 400 km $\log (E_{3640}/E_{3500}) = 0.14$ and gives $T_e = 4000^\circ$ K. In order to have $T_e = 12,000^\circ$ K we would have to have $\log (E_{3640}/E_{3500}) = 0.05$. The chances for this much error in the data are very small, but not nil. Since the values of N_e and $\frac{\partial \ln N_e}{\partial h}$ depend upon the values of T_e and $\frac{\partial \ln T_e}{\partial h}$ respectively, they are also poorly defined by the data.

The Balmer continuum data show consistently that $\frac{\partial \ln T_e}{\partial h} > 0$. The probable errors are such that $\frac{\partial \ln T_e}{\partial h}$ could be zero, but the chances for this are slight. The values of $\frac{\partial \ln T_e}{\partial h}$ in Table 7 depend upon the values of T_e and they have undoubtedly been overestimated in the higher chromospheric levels by the use of straight lines to fit the data. On the other hand, there is nothing in this method that could give $\frac{\partial \ln T_e}{\partial h} > 0$ if this were not actually the case.

If we assume constant temperature, the value of $\frac{d \ln N_e}{dh}$ is -1.1 x 10^{-8} cm^{-1}. This value is considerably higher than the value found by Cillié and Mensel[2] from the 1932 data. The values of N_e determined from equation (38) with T_e= 15,200° K are listed in the last row of Table 7. The value of 15,200° K for T_e was used because, as will be shown below, it is the temperature given by the assumption of an isothermal chromosphere in hydrostatic equilibrium.

Table 7

T_e, $\frac{d \ln T_e}{dh}$, N_e and $\frac{d \ln N_e}{dh}$.

Height (km) / T_e° K	400	800	1200	1600	2000	2400	$\frac{1}{2}\frac{d \ln T_e}{dh}$ x 10^{-8} cm^{-1}
λλ3640-3600	2,600	3,400	4,420	6,300	14,700		2.03
λλ3640-3550	3,890	4,590	5,320	6,300	8,400	12,650	0.89
λλ3640-3500	4,000	4,680	5,490	6,630	8,830	13,250	0.88
λλ3600-3550	6,300	6,300	6,300	6,300	6,300	6,300	0
λλ3600-3500	5,000	5,480	6,060	6,760	7,690	8,900	0.43
λλ3550-3500	3,900	4,850	5,840	7,270	8,800	14,570	0.86
AVR.	4,280	4,880	5,570	6,590	9,120	11,130	0.85
$\frac{d \ln T_e}{dh}$ x 10^8 cm^{-1}	0.36	0.41	0.47	0.56	0.77	0.95	
$\frac{d \ln N_e}{dh}$ x 10^8 cm^{-1}	-0.83	-0.80	-0.74	-0.68	-0.53	-0.38	
N_e x 10^{11}	4.2	3.0	2.2	1.5	1.3	0.93	
N_e x 10^{11} (T_e=15,200°)	11.0	7.1	4.6	3.0	1.9	1.2	

B. Hydrostatic Equilibrium

It is interesting to compare the relationships among T_e, $\frac{d\ln T_e}{d\tau}$ and $\frac{d\ln N_e}{d\tau}$ in Table 7 with the relationships derived from the assumption of hydrostatic equilibrium. In this section we describe the results of such comparisons, which showed that the data are not strongly inconsistent with the assumption of hydrostatic equilibrium, but that the assumption of an isothermal chromosphere is untenable.

Since the chromosphere is predominently hydrogen and the largest percentage of the remaining atoms are helium, which has a high ionization potential, we have

$$N_p \cong N_e$$

Hence, the equation of hydrostatic equilibrium is

$$dp = -(N_e + N_H) m_H g \, dh, \tag{44}$$

and the ideal gas law can be written

$$p = (2N_e + N_H) k T_e. \tag{45}$$

If we define

$$\eta = \frac{N_e}{N_e + N_H} \tag{46}$$

as a fraction of hydrogen ionized, we get

$$dp = -\frac{N_e}{\eta} m_H g \, dh \tag{47}$$

and

$$p = \left(1 + \frac{1}{\eta}\right) N_e k T_e. \tag{48}$$

From (47) and (48), we get

$$\frac{d \ln N_e}{d\lambda} + \frac{d \ln T_e}{d\lambda} - \frac{1}{\eta+1} \frac{d \ln \eta}{d\lambda} + \frac{m_H g}{(\eta+1) k T_e} = 0 . \qquad (49)$$

For $\eta \ll 1$,

$$\frac{d \ln \eta}{d\lambda} = - \frac{d \ln (N_H / N_e)}{d\lambda} .$$

If we assume thermodynamic equilibrium as an approximation, then the ionization equation gives

$$\frac{N_H}{N_e} \propto N_e \, T_e^{-3/2} \, e^{15.7 \times 10^4 / T_e}$$

and

$$\frac{d \ln \eta}{d\lambda} = - \frac{d \ln N_e}{d\lambda} + \left(\frac{3}{2} + \frac{15.7 \times 10^4}{T_e} \right) \frac{d \ln T_e}{d\lambda} . \qquad (50)$$

Substituting (50) and (43) in (49) and setting $\eta = 0$, we get

$$\left(1 - \frac{15.7 \times 10^4}{T_e} \right) \frac{d \ln T_e}{d\lambda} + \frac{m_H g}{k T_e} + \frac{d \ln C_{3640}}{d\lambda} = 0 . \qquad (51)$$

Equation (51) can be written

$$(T_e - 15.7 \times 10^4) \frac{d T_e}{d\lambda} + \frac{d \ln C_{3640}}{d\lambda} T_e^2 + \frac{m_H g}{k} T_e = 0 .$$

If we consider $\frac{d \ln C_{3640}}{d\lambda}$ as constant and use the value given by equation (34a), this equation admits to the integral

$$\frac{T_e^{4.1}}{15,200 - T_e} = K \, e^{2.24 \times 10^{-5} \lambda} , \qquad (52)$$

and equation (51) can be written

$$\frac{d \ln T_e}{d\lambda} = 2.19 \times 10^{-5} \left(\frac{15,200 - T_e}{157,000 - T_e} \right) . \qquad (53)$$

The Balmer continuum data gives values of $\frac{d \ln T_e}{dh}$ and T_e, as given in Table 7. The values in the low chromosphere give $n \ll 1$ and equations (52) and (53) should apply. We tabulated in Table 8 the values of $\frac{d \ln T_e}{dh}$ obtained from (53), by using the values of T_e from Table 7. These values are considerably lower than the values in Table 7. Hence, the use of the values of $\frac{d \ln T_e}{dh}$, T_e and $\frac{d \ln N_e}{dh}$ in Table 7 gave, under conditions of hydrostatic equilibrium, too low values for $\frac{d \ln \epsilon_{2640}}{dh}$, the observed emission gradient. However, it is clear that a relatively slight modification of the parameters of Table 7 would permit us to satisfy the condition of hydrostatic equilibrium.

If the chromosphere is not in hydrostatic equilibrium, it is much more likely to be too extended rather than too compressed, and thus to be out of equilibrium in the direction opposite to that indicated. This result suggests then, that our values for T_e and $\frac{d \ln T_e}{dh}$ are inconsistent. The inconsistency most likely arises from the use of straight lines to represent the variation of $\log E_\lambda$ with height. We note that equation (53) gives an upper limit for $\frac{d \ln T_e}{dh}$ of $0.21 \times 10^{-8} cm^{-1}$ and that $\frac{d \ln T_e}{dh}$ decreases as T_e increases. This is, of course, a result of the assumption that the ionization is low and that the emission decreases exponentially with height.

Table 8

Height (km)	400	800	1200	1600
$\frac{d \ln T_e}{dh} \times 10^8 cm^{-1}$	0.16	0.15	0.14	0.12

Alternatively, we can look at the data for $h \geq 2000$ km, where the Balmer continuum data give $n \gtrsim 1$. In this case $\frac{d \ln n}{dh} \gtrsim 0$ and equation (49) becomes

$$\frac{\partial \ln N_e}{\partial h} + \frac{\partial \ln T_e}{\partial h} + \frac{m_H g}{k T_e} = 0. \tag{54}$$

Using (43), we get

$$\frac{3}{4}\frac{\partial \ln T_e}{\partial h} + \frac{1}{2}\frac{\partial \ln \varepsilon_{5460}}{\partial h} + \frac{m_H g}{2 k T_e} = 0, \tag{55}$$

which can be written

$$\frac{\partial T_e}{\partial h} + \frac{2}{7}\frac{\partial \ln \varepsilon_{5460}}{\partial h} T_e + \frac{2}{7}\frac{m_H g}{k} = 0. \tag{56}$$

The integral of this equation with $\frac{\partial \ln \varepsilon_{5460}}{\partial h} = -2.19 \times 10^{-8}\ \mathrm{cm}^{-1}$ gives

$$T_e = C\, e^{0.62 \times 10^{-8} h} + 15,200 \tag{57}$$

and

$$\frac{\partial \ln T_e}{\partial h} = \frac{0.62 \times 10^{-8}}{1 + \frac{15,200}{C} e^{-0.62 \times 10^{-8} h}}. \tag{58}$$

If $\frac{\partial \ln T_e}{\partial h} > 0$ as our data in Table 7 indicate, hydrostatic equilibrium thus shows us that $T_e > 15,200^\circ$ K, and that $\frac{\partial \ln T_e}{\partial h}$, the gradient itself, increases upward.

The usual method of applying hydrostatic equilibrium considerations to the chromosphere[5] is to assume T_e = const. and $\eta \gg 1$. If we make this assumption, in spite of the gradient shown in Table 7, and set C = 0 in (57), we get $T_e = 15,200^\circ$ K. (For the emission-height gradients obtained by Gillie and Mansel, a $T_e = 22,500^\circ$ K is required on this assumption.) We have already shown that it is difficult to reconcile the Balmer continuum data for the chromosphere below 1000 km with $T_e = 15,200^\circ$ K, and thus on the isothermal model are forced to admit rather wide departures from

hydrostatic equilibrium.

The above analysis of the Balmer continuum data for a chromosphere in hydrostatic equilibrium is rather crude, but nevertheless leads to conclusions of some interest. The most likely model of the chromosphere that satisfies both the data and the assumption of hydrostatic equilibrium is the following:

$$T_e < 12,000^\circ K \quad \text{for} \quad h < 1000\ km.$$

$$\frac{d \log T_e}{dh} > 0 \quad \text{and} \quad \frac{d \log N_e}{dh} = -1.1 \times 10^{-8} + \tfrac{1}{4} \frac{d \log T_e}{dh}.$$

$$N_e \sim 10^{11}.$$

The more thorough analysis of the continuum data which is now in progress should allow more specific definition of T_e and $\frac{d \log T_e}{dh}$.

C. Balmer Line Emission

Analysis of the line emission of the hydrogen Balmer spectrum can give us results on self-absorption and departures from thermodynamic equilibrium. We consider first the general form of our approach to these problems.

The graphs of log E_n vs. height of the moon's limb shown in Figure 8 indicate that above a certain level the emission decreases approximately exponentially with height. For the lines H_{12} to H_{11}, the exponential approximation is good above 600 km. For the lower order lines, the same approximation is not good until one goes to higher levels. At H_8 the approximation is good above 2000 km. In these ranges the data for each line are adequately represented by exponential relationships. If departures from such exponentials of real physical significance existed, they would affect

the curves for adjacent n values in such a way as to produce systematic departures from the exponential that progressed continuously with n. No evidence for such progressive departure is exhibited by the curves.

In the highest order lines the effects of self-absorption and departures from thermodynamic equilibrium are probably small. Theoretical computations of the b_n's by Thomas[21] and Matsushima[24] show that they approach one as n increases. Although the computations include only $n \leq 10$, it is obvious that by the time n reaches about 25 the b_n's will be very close to unity.

Since the absorption coefficient, a_ν is well known (Thomas[7]) varies as $1/n^3$, the amount of absorption in the higher order lines will be small compared to that in the lower order lines. As a first approximation we can assume that the absorption term becomes negligibly small for $n \geq 28$. On this basis we would then expect that the observed emission from the lines for $n \geq 28$ would be very nearly a true representation of the population of the level n as predicted by thermodynamic equilibrium theory.

Unfortunately, all of the lines for $n \geq 28$ are affected by blends. H_{28} and H_{30} are blended with unresolved metal lines. The wings of these lines overlap with H_{29} and H_{31} and so the blends also affect the intensities of these lines. However, the primary interest in these higher order lines is to obtain an emission gradient that is free from the perturbing effects of self-absorption and departures from thermodynamic equilibrium. For this case, we have, from equation (26),

$$\varepsilon_n = h C_n N_e^2 T_e^{-3/2} e^{\chi_n}, \qquad (59)$$

and at the head of the Balmer continuum ($n = \infty$)

$$\mathcal{E}_\infty = h C_\infty N_e^2 T_e^{-3/2}. \qquad (60)$$

Hence, we can use the emission gradient at the head of the Balmer continuum as a reference from which to measure the perturbations in the emission gradients. The observed gradients will have the form

$$\frac{\partial \ln E_n}{\partial \lambda} = -\beta_n = \frac{\partial \ln E_\infty}{\partial \lambda} - \chi_n \frac{\partial \ln \tau_\lambda}{\partial \lambda} + \frac{\partial \ln b_n}{\partial \lambda} + \gamma_n(h) \qquad (61)$$

where the term $\gamma_n(h)$ is the change in the gradient caused by self-absorption and hence, is a function of height. The observations show that to a good approximation

$$\frac{\partial \ln E_\infty}{\partial \lambda} = \text{const.} = -2.19 \times 10^{-8}\ \text{cm}^{-1}.$$

The observed values of β_n tabulated in Table 4 change systematically with n and h. However, above 2000 km the values are no longer dependent upon h, or, more correctly, the dependence upon h is too small to be shown by the data. In general, the last three terms on the right of equation (61) depend upon both h and n. The absence of a dependence upon h means either that the important terms are independent of h or that the dependence on h cancels out. The values of $\beta_\infty - \beta_n$ are not small for the lower order lines. In fact, for H_9 above 2000 km we have $\beta_\infty - \beta_9 = 0.68 \times 10^{-8}\ \text{cm}^{-1}$, and we are forced to conclude that most of this difference comes from terms or combinations of terms that are slowly varying functions of height. The term $-\chi_n \frac{\partial \ln \tau_\lambda}{\partial \lambda}$ is of the wrong sign if $\frac{\partial \ln \tau_\lambda}{\partial \lambda} > 0$. The Balmer continuum data leave little doubt that this is the case, and we must attribute the difference to the other two terms. Clearly $\gamma_n(h) > 0$ so we

will investigate this self-absorption term first.

1. Self-absorption.

The observed emission in a line is

$$E_n = A V_n A_{n,1} \int_{\lambda} \int_{-\infty}^{\infty} N_n \, e^{-\alpha_{n,1} \int_{\infty}^{z} N_1(x,y,z)\, dz} \, dy \, dx. \tag{62}$$

The observations for the higher order lines give

$$E_n = E_{n,0} \, e^{-\beta_n h}.$$

If we assume that the emission gradients in these lines are unaffected by self-absorption, then we can write

$$N_n = N_{n,0} \, e^{-\beta_n h} \tag{63}$$

as a first approximation.

Matsushima[25] has shown that for this approximation

$$E_n = \frac{(2\pi\sigma)^{1/2}}{\beta_n \sqrt{\gamma_n}} A V_n A_{n,1} N_n \sum_{m=0}^{\infty} (-1)^m \frac{\left(1 + \frac{\beta_1 m}{\beta_n}\right)^{-1}}{(1+m)^{3/2}} \frac{(\bar{N}_2 \alpha_{n,1})^m}{m!} \tag{64}$$

where $\bar{N}_2$ is the total number of atoms in the Balmer ground state along the line of sight. The effect of the absorption on the observed emission gradient is

$$\gamma_n(h) = \frac{\partial \log A V_n}{\partial h} = \beta_n \bar{N}_2 \alpha_{n,1} \frac{\sum_{m=1}^{\infty} (-1)^{m+1} \frac{(1+\beta m)^{-1}}{(1+m)^{3/2}} \frac{(\bar{N}_2 \alpha_{n,1})^{m-1}}{(m-1)!}}{\sum_{m=0}^{\infty} (-1)^m \frac{(1+\beta m)^{-1}}{(1+m)^{3/2}} \frac{(\bar{N}_2 \alpha_{n,1})^m}{m!}} \tag{65}$$

where $\beta = \frac{\beta_2}{\beta_n}$ and is considered to be constant. It follows that

$$\gamma_n(h) = \frac{\beta_n \bar{N}_2 \alpha_{n,1}}{(1+\beta) 2^{3/2}} \left\{ 1 + \left[\frac{1}{(1+\beta) 2^{3/2}} - \frac{(1+\beta) 2^{3/2}}{(1+2\beta) 3^{3/2}} \right] \bar{N}_2 \alpha_{n,1} \right. \tag{66}$$

$$\left. + \left[\frac{1}{(1+\beta)^2 4^{3/2}} - \frac{1}{(1+2\beta) 2^{3/2}} + \frac{(1+\beta)}{(1+3\beta) 2^{3/2}} \right] (\bar{N}_2 \alpha_{n,1})^2 + \cdots \right\}.$$

$\gamma_n(h)$ is the change in β_n caused by self-absorption. Since N_2 is exponential in h, we also have $\gamma_n(h)$ changing approximately exponentially with height. The only evidence for such changes occurs in the emission from H_8 to H_{11}, and then only in the levels below 2000 km. Apparently, then, self-absorption is either a relatively small effect and is not affecting the height gradients above 2000 km or the b_n term is entering in such a way that it partly compensates for the change with h. Since there are obvious changes in β_n which are not of the form of (66), we must have a significant contribution from the b_n term. However, before we consider this term, it is helpful to estimate β_2 and $\bar{N}_2$ from the effects which are apparently caused by self-absorption.

We note that if we again use the exponential form for N_n (64) can be written

$$\log E_n = \log E_{n,0} - 0.434\,\beta_n h + \log A_{bs}. \tag{67}$$

where

$$\log A_{bs} = \log\left[1 - \frac{\bar{N}_2 \alpha_{n,2}}{(1+\beta)\,3^{N_2}} + \frac{(\bar{N}_2 \alpha_{n,2})^2}{2!(1+2\beta)\,3^{N_2}} - \frac{(\bar{N}_2 \alpha_{n,2})^3}{3!(1+3\beta)\,3^{N_2}} + \cdots\right]. \tag{68}$$

We have seen from equation (66) that the effect of self-absorption is to change the emission gradient by an amount which changes exponentially with height. Hence, as a first approximation we will interpret all of the departures from an exponential decrease of emission with height as being due to self-absorption. If this interpretation is legitimate, then from (68) and the observed emission in, say, H_9 we should be able to get approximate values for β_2 and $\bar{N}_{2,0}$. From the first two terms on the right of (68) and the observed intensities in H_9, we estimate $\beta_2 = 1.5 \times 10^{-8} cm^{-1}$. The

coefficients of the terms in (68) do not depend too strongly upon the values of β_2 so long as we keep it reasonably close to β_9. The observed value of β_9 is $1.51 \times 10^{-8} cm^{-1}$. If we use the estimated value of β_2 in the coefficients of (68) we can write

$$\log \text{Abs.} = \log \left[1 - \frac{N_2 a_{m,2}}{2 N_e} + \frac{(N_2 a_{m,2})^2}{2! \, 3 N_e} - \frac{(N_2 a_{m,2})^3}{3! \, 4 N_e} + \cdots \right]. \quad (69)$$

For a particular value of log Abs., equation (69) can be solved for $N_2 a_{m,2} = N_{2,0} a_{m,2} e^{-\beta_2 h}$.

The plot of log E_9 vs. height in Figure 8 was fitted with an empirical curve. Above 2000 km the curve was approximated by a straight line. If we extend this straight line portion to lower heights and attribute the differences between the two curves to self-absorption, we get the values of log Abs. tabulated in row 2 of Table 9. The values of log $\bar{N}_2 a_{9,2}$ in row 3 of Table 9 were obtained from equation (69) and the values of log Abs. in row 2. The values of log $\bar{N}_2 a_{9,2}$ in Table 9 are plotted against height in Figure 11. The resulting curve is a straight line from which we get $\beta_2 = 2.19 \times 10^{-8} cm^{-1}$ and $\bar{N}_{2,0} a_{9,2} = 10$. We note, however, that there is a good chance that this method gives erroneous values of log Abs. since we have ignored the b_n term in (61). Indeed, we shall see later that we have underestimated the absolute values of log Abs., and that our value of β_2 is much too large. It does not necessarily follow that $\bar{N}_{2,0} a_{9,2}$ is too small since decreasing β_2 will have the effect of increasing log Abs. at heights greater than zero. The theoretical value of $a_{9,2}$ is 1.51×10^{-15}. For $\bar{N}_{2,0} a_{9,2} = 10$, we get $\bar{N}_{2,0} = 6.6 \times 10^{15}$ and for $\beta_2 = 1.5 \times 10^{-8} cm^{-1}$ the number of N_2 atoms per cm^3 at the base of the chromosphere is 1.2×10^6.

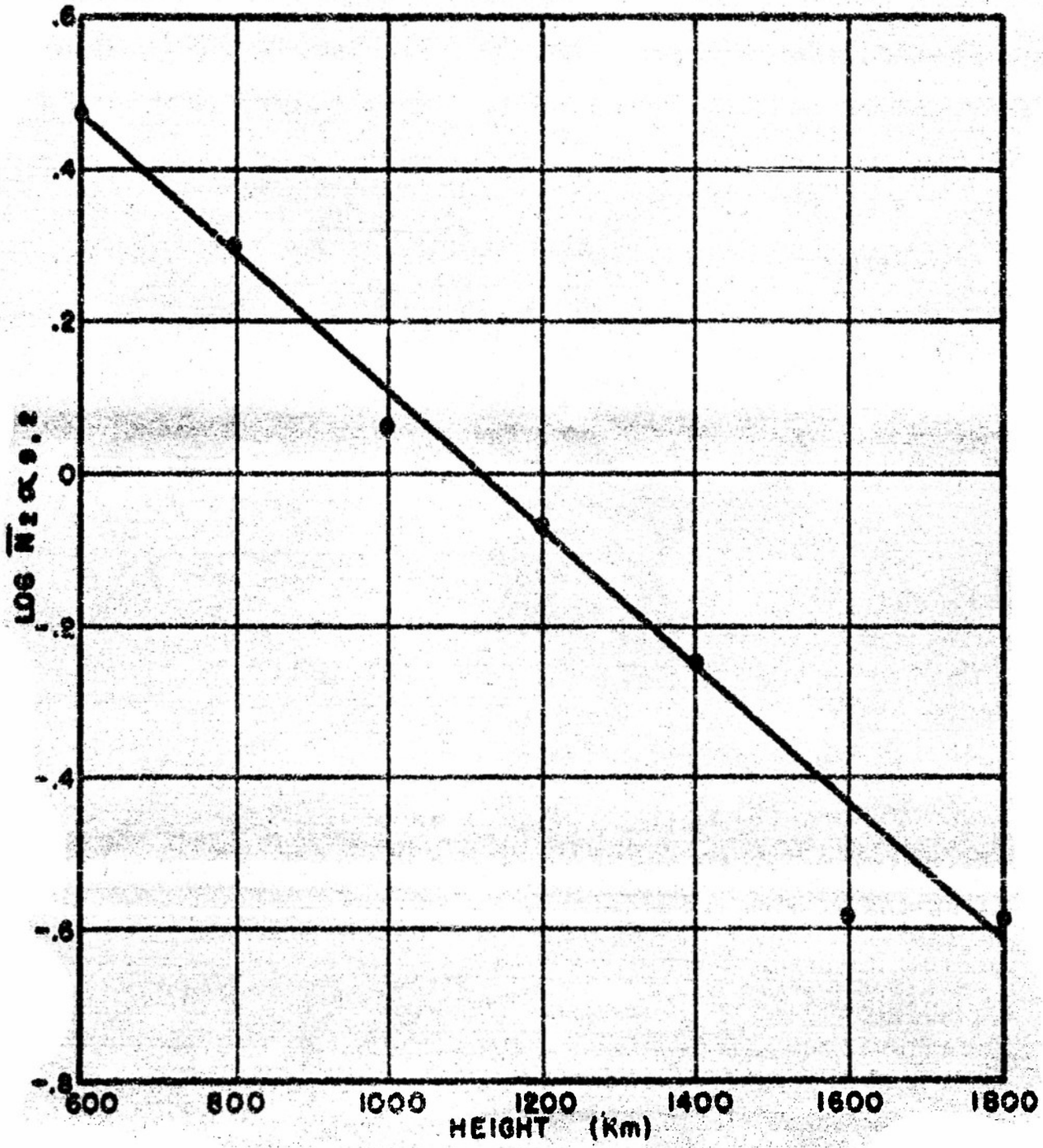

FIG. 11 LOG $\bar{N}_2 \alpha_{9.2}$ VS HEIGHT

Table 9

log Abs and $\bar{N}_2 a_{n,2}$

Height (km)	600	800	1000	1200	1400	1600	1800
log Abs.	-0.18	-0.13	-0.08	-0.06	-0.04	-0.02	-0.02
log $\bar{N}_2 a_{9,2}$	0.47	0.30	0.06	-0.07	-0.25	-0.69	-0.69

2. b_n Gradients.

We have pointed out above that the changes in the β_n with n cannot be the result of self-absorption alone and thus are at least partly, and possibly entirely, due to the term $\frac{\partial \ln b_n}{\partial h}$. Omitting the absorption term in (61), we get

$$\frac{\partial \ln b_n}{\partial h} = \beta_{n+1} - \beta_n + \chi_n \frac{\partial \ln T_e}{\partial h} \qquad (70)$$

The last term in this equation is unknown. However, we can estimate it from the Balmer continuum data. In the low chromosphere we have $\frac{\partial \ln \bar{N}_2}{\partial h}$ $\approx 0.4 \times 10^{-5}$ cm^{-1} and $T_e = 5000°$, whereas at 2400 km $\frac{\partial \ln \bar{N}_2}{\partial h} \approx 1 \times 10^{-5}$ cm^{-1} and $T_e = 11{,}000°$ (see Table 7). The large value for $\frac{\partial \ln T_e}{\partial h}$ at the higher levels is due to the use of straight lines for the emission gradients in the Balmer continuum. In the higher chromosphere we expect a high degree of ionisation and from equation (57) we see that the assumption of hydrostatic equilibrium gives $\frac{\partial \ln T_e}{\partial h}$ increasing with height in order to maintain a constant emission gradient. On the other hand, the assumption of low ionization and hydrostatic equilibrium in the low chromosphere gave $\frac{\partial \ln T_e}{\partial h}$ decreasing with height. The precise values are not too important since the χ_n term is small for $n \geq 6$. For use in equation (70) at 2400 km, we

take T_e=16,000° and $\frac{d \ln T_e}{d h} = 0.4 \times 10^{-8}$ cm^{-1}. Whence,

$$\frac{d \ln b_n}{d h} = \beta_{cn} - \beta_n + \frac{4.8 \times 10^{-8}}{n^3} \qquad (71)$$

The value of $\beta_{cn} = 2.19 \times 10^{-8}$ was obtained from the emission at the head of the Balmer continuum. The values of β_n are tabulated in Table 4 and the apparent values of $\frac{d \ln b_n}{d h}$ are tabulated in Table 10. Since the β_n do not change with height except in the low order lines, these values of $\frac{d \ln b_n}{d h}$ apply at all levels covered by the observations except those below 600 km where the observations are incomplete. The apparent values of $\frac{d \ln b_n}{d h}$ for $n \geq 8$ are represented approximately by the equation

$$\frac{d \ln b_n}{d h} = 1.74 \times 10^{-8} e^{-0.091 n} \qquad (72)$$

as shown in Figure 12.

If we integrate equation (72), we get

$$\ln b_n = 1.74 \times 10^{-8} e^{-0.091 n} h - f(n). \qquad (73)$$

Since all of the b_n's must be unity at the height, h_0, at which the electron temperature and radiation temperature are the same, (73) can be written

$$\ln b_n = 1.74 \times 10^{-8} e^{-0.091 n} (h - h_0). \qquad (74)$$

The relative values of the apparent b_n's can be determined from the differences between the observed Balmer decrements and the thermodynamic equilibrium decrements. In the case of thermodynamic equilibrium we use equations (23) and (24) to compute the Balmer decrements. Since the decrements are defined as $\ln \left(\frac{\epsilon_{mn}}{\epsilon_{mn}^*} \right)$, we have the thermodynamic equilibrium

FIG. 12 EMPIRICAL FIT OF $1.74 \times 10^{-8} e^{-0.091n}$ TO OBSERVED VALUES OF $\frac{\partial \ln b_r}{\partial h}$

Table 10

Apparent Values of $\frac{\partial \ln b_n}{\partial h}$ and Balmer Decrements

H_n	$\frac{\partial \ln b_n}{\partial h}$ $\times 10^6 cm^{-1}$	$(\chi_n + \ln C_n) - (\chi_{10} + \ln C_{10})$	$\ln (C_n/C_{10})$ 1000 km	2000 km	3000 km	4000 km
8	0.87					
9	0.74	2.65	1.77**	2.17	2.57	2.97
10	0.68	2.28	1.49**	1.84	2.29	2.64
11	0.61	1.96	1.24**	1.61	1.90	2.19
12	0.54	1.65	1.21	1.44	1.67	1.90
13	0.54	1.39	1.05	1.28	1.51*	1.74*
14	0.51	1.15	.91	1.12	1.33*	1.54*
15	0.47	.92	.62	.80	.96*	1.16*
16	0.47	.72	.45	.63	.81*	.99*
17	0.42	.52	.56	.58	.70*	.82*
18	0.36	.30	.21	.27	.33*	.39*
19	0.30	.17	.23	.23	.23*	.23*
20	0.30	- 0	0	0	0*	0*
21	0.25	- .16	- .07	- .13		
22	0.24	- .29	- .27	- .32		
23	0.24	- .42	- .41	- .46		
24	0.15	- .56	- .50	- .64		
25	0.12	- .68	- .55	- .72		
26	0.15	- .80	- .76	- .89		
27	0.12	- .91	- .87	-1.04		
28	0.08	-1.03	- .84	-1.05		
29	0.12	-1.14	-1.10	-1.27		
30	0.08	-1.24	- .88	-1.09		
31	0.07	-1.34	-1.36	-1.57		

** Corrected for apparent self-absorption

* Extrapolated from lower levels

decrements given by $(\chi_m + \ell_m C_m) - (\chi_{m'} + \ell_{m'} C_{m'})$. The values of $(\chi_m + \ell_m C_m) - (\chi_{2\alpha} - \ell_{2\alpha} C_{2\alpha})$ at 6000° are tabulated in column 3 of Table 10, and the observed values of $\ell_m \left(\frac{\epsilon_m}{\epsilon_{2\alpha}}\right)$ are tabulated in columns 4 to 8. The values of $A_{n,2}$ in the C_n have been tabulated by Menzel and Pekeris[26].

The observed values of $\ell_m \left(\frac{\epsilon_m}{\epsilon_{2\alpha}}\right)$ appear to give the best general agreement with the predicted decrements at h = 3000 km. However, we note that in the higher order lines for h ≥ 2000 km all of the observed decrements exceed the predicted decrements whereas in the lower order lines the reverse is true for h ≤ 3000 km. Above 3000 km the observed decrements exceed the predicted decrements for all lines. This is strongly suggestive that self-absorption is affecting the intensities of the lower order lines even in the higher levels and that the b_n's are greater than one down to at least 2000 km. Our purpose in this section, however, is to attempt to describe all of the observations in terms of b_n's so we continue to ignore self-absorption and see how far we can go.

The apparent values of $\ell_m \left(\frac{b_m}{b_{2\alpha}}\right)$ are listed in Table 11. The values given by equation (74) are ± 0.42 for $h - h_0 = \pm$ 1000 km and ± 0.84 for $h - h_0 = \pm$ 2000 km. The agreement of these values with the observed values is very good if we set h_0 = 3000 km. But, it should be recognized that the values in Table 11 are obtained from the observed Balmer decrements, and the changes in the decrements are caused by the difference in the emission gradient from which equation (74) was derived so we should expect consistency.

Table 11

Apparent $\ell_m (b_{12}/b_{2\alpha})$

1000 km	2000 km	3000 km	4000 km
-0.79	-0.44	+0.01	+0.36

The decrements in the integrated emission are larger than the decrements in the emission per unit volume and they begin to exceed the predicted decrements at levels well below 2000 km. The effects are much too large to be due to temperature changes and we are forced to conclude that the values of b_n averaged over the chromosphere above 2000 km are greater than one.

Thomas[27] has shown that $b_n > b_{n+k}$ when the electron temperature is greater than the radiation temperature and $b_n < b_{n+k}$ when the reverse is true. Hence, on the basis of our present model we should expect to find an electron temperature of about 6000° K at 3000 km with lower temperatures at lower levels and higher temperatures above. The Balmer continuum data suggest this sort of model and up to this point our model is consistent. Fortunately, there is a critical way of checking the consistency of our interpretation. Wildt[19] has used a method of getting an emission gradient which is based on the heights at which the various lines reach equal intensity. However, his results gave anomalously low values for the gradients. Thomas[7] has interpreted this anomalous emission gradient as a manifestation of the fact that $b_n > b_{n+k}$. We should be able to check the consistency of our interpretation of the effects of the b_n by analysing the method used by Wildt. Hence, if we put $h_0 = 3 \times 10^8$ in equation (74) we get

$$\ln \epsilon_{mn} = 1.74 \times 10^{-9} (h - 3 \times 10^8) e^{-0.69 m}, \qquad (75)$$

and, if our model is right, we should expect this equation to be consistent with whatever results we get.

The condition for equal intensity in all of the Balmer lines is

$$\frac{d \ln \epsilon_{mn}}{dh} = 0. \qquad (76)$$

From (30) and (36), we get

$$\sigma + a \frac{\partial \ln \kappa_\lambda}{\partial \lambda} - \frac{1}{2} \frac{\partial \ln \tau_\lambda}{\partial \lambda} + \frac{\partial \chi_m}{\partial \lambda} + \frac{\partial \ln b_m}{\partial \lambda} = 0 \qquad (77)$$

where

$$\sigma = \frac{\partial}{\partial \chi_m} (\ln C_m - \chi \ln \beta_m) \frac{\partial \chi_m}{\partial h}. \qquad (78)$$

Wildt assumed T_e = const. and ignored the b_m and β_m terms. He then interpreted the value of σ as $2 \frac{\partial \ln \kappa_\lambda}{\partial \lambda}$. The value of $\frac{\partial \ln \kappa_\lambda}{\partial \lambda}$ obtained by this method was considerably smaller than the value obtained by Cillié and Mensel[2] by the more direct method of plotting log E_λ against height. Cillié and Mensel made the same assumptions as Wildt and the data that they used were also used by Wildt. Thomas interpreted this difference as being due to $b_m > b_{m+1}$ and, therefore, $\frac{\partial \ln b_m}{\partial m} < 0$. We see from equation (77) that this interpretation is not completely justified without further qualification. The discrepancy clearly arises from the terms in (77) which have been neglected. But, Wildt has neglected the last term in (77) which, when expanded, is

$$\frac{\partial \ln b_m}{\partial \lambda} + \frac{\partial \ln b_m}{\partial m} \frac{\partial m}{\partial \lambda}.$$

Our attempts to account for the changes in the emission gradients by self-absorption showed that, considering the first term, $\frac{\partial \ln b_m}{\partial \lambda} > 0$ and non-negligible. It may well be, however, that the $\frac{\partial \ln b_m}{\partial m} < 0$, so that the second term is helping to account for the discrepancy. Without investigating the first term it is impossible to tell whether or not this is the case. In fact, since the emission gradients are different for each line the values of $\frac{dn}{dh}$ will depend upon the particular intensity we are

considering. As an illustration of this we have plotted in Figure 13 the heights of equal intensity against $h_m C_m - \frac{1}{2} h_m R_m$ for three different intensities. In all cases we get straight lines, but for the intensity of H_β at 4000 km $\sigma = 1.68 \times 10^{-8} cm^{-1}$, for the intensity of H_β at 3000 km $\sigma = 1.88 \times 10^{-8} cm^{-1}$, and for the intensity of H_β at 2000 km $\sigma = 2.19 \times 10^{-8} cm^{-1}$. We have shown that these changes are not entirely due to self-absorption and part of the change must be attributed to the $\frac{dh_m b_m}{dh}$ term.

The surprising thing is that the values of σ are independent of n. From equations (43) and (77), we see that

$$2.19 \times 10^{-8} \sigma = -\frac{2\chi_m}{m} \frac{dh_m}{dh} - \chi_m \frac{dh_m R_m}{dh} + \frac{dh_m b_m}{dh} + \frac{dh_m b_m}{dm} \frac{dm}{dh} \quad (79)$$

The left side of (79) is independent of n but the first three terms on the right, if we use equation (75), all change rapidly with n. On the other hand, the values of $\frac{dn}{dh}$ obtained from the data are very well represented by

$$\frac{dm}{dh} = a e^{0.0775 m} \quad (80)$$

where $a = -2.45 \times 10^{-8} cm^{-1}$ if we use the intensity of H_β at 4000 km but has different values for different intensities. Equation (75) gives

$$\frac{dh_m b_m}{dm} = -0.158 \times 10^{-8} e^{-0.0775 m} \left(\frac{1}{\lambda} - 3 \times 10^{-8}\right) \quad (81)$$

Hence, the term $\frac{dh_m b_m}{dm} \frac{dm}{dh}$ depends on n mostly through the value of h associated with n. For n's where $h > 3000$ km this term is negative and for n's where $h < 3000$ km it is positive. We note, however, that the χ_m terms in (79) are negligibly small and that the apparent $\frac{dh_m b_m}{dh}$ are positive and approaching zero for large n. Furthermore, the apparent value of $\frac{dh_m b_m}{dh}$ is greater than $2.19 \times 10^{-8} \sigma$ for $n \leq 18$ and less than this value for

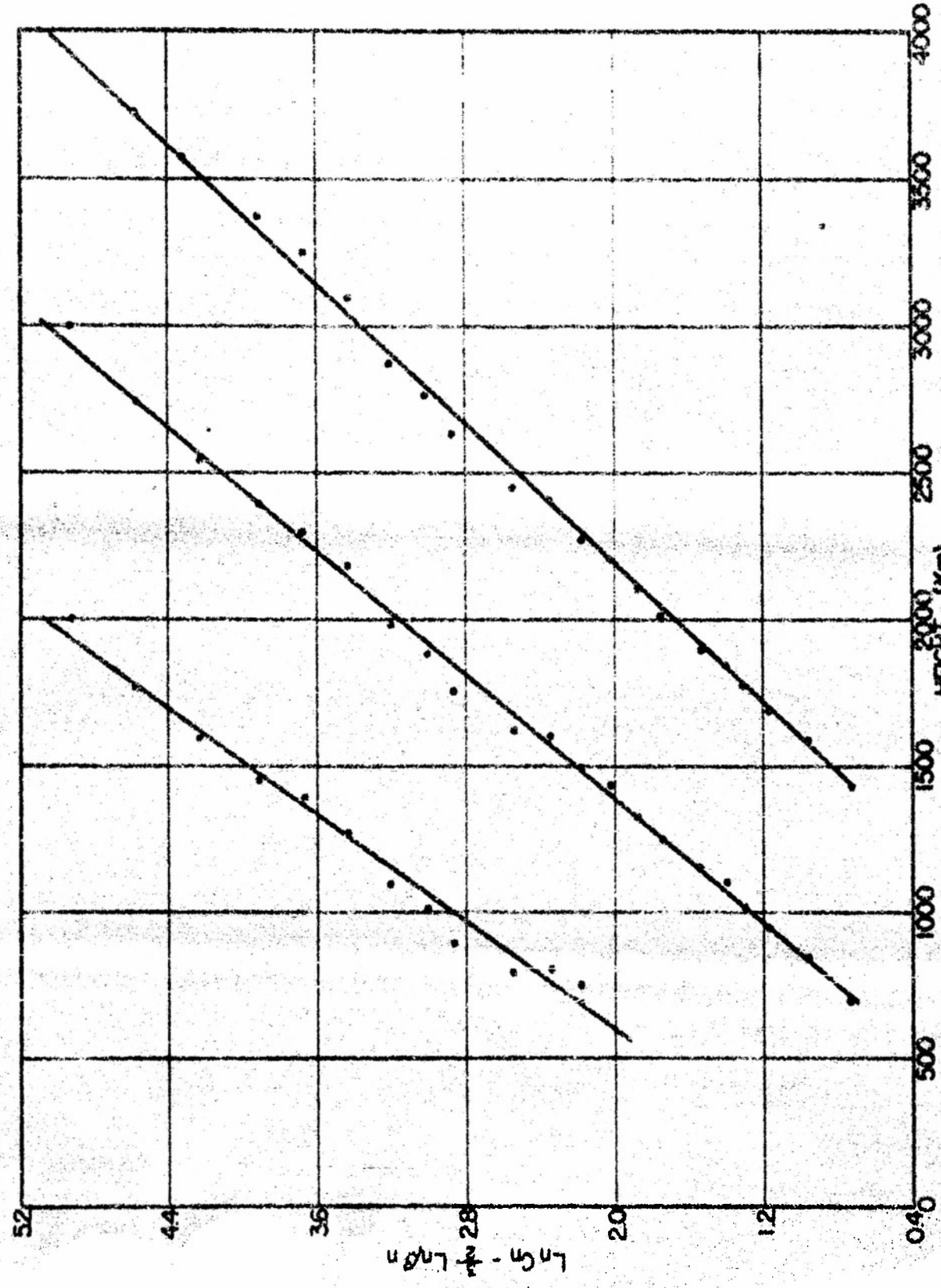

FIG 13 $\ln\sigma_n - \frac{1}{2}\ln\beta_n$ VS HEIGHT

$n > 18$. Hence, we should have $\frac{\partial \ln b_n}{\partial n} > 0$ for $n > 18$ and $\frac{\partial \ln b_n}{\partial n} > 0$ for $n \leq 18$. This is just the opposite of the results given by equation (75). The result that $\frac{\partial \ln b_n}{\partial n} < 0$ for large n and > 0 for small n is unacceptable from a physical standpoint and we are forced to include the effects of self-absorption in order to remedy the situation. We note that the only remedy is to have $\frac{\partial \ln b_n}{\partial n} < 0$ for all n since the effect of self-absorption is to decrease $\left|\frac{\partial \ln b_n}{\partial n}\right|$ in the low order lines. This shows conclusively that equation (75) is inconsistent with the observations in that it gives b_n's less than one.

As a further illustration of the inconsistency of equation (75) we include the χ_λ terms in (79) and use (75) to evaluate $\frac{\partial \ln b_n}{\partial n}$ and $\frac{\partial \ln b_n}{\partial h}$. We then have an equation of the form

$$\frac{\partial \ln \tau_\lambda}{\partial h} = A + B\,\tau_\lambda. \qquad (82)$$

By evaluating the constants A and B for all n at two different intensities we get two values of A and B at some heights and we can solve for τ_λ and $\frac{\partial \ln \tau_\lambda}{\partial h}$. In all cases the solutions give τ_λ negative and $\frac{\partial \ln \tau_\lambda}{\partial h} > 1 \times 10^{-8}\ \text{cm}^{-1}$. Obviously, then, we cannot correct the inconsistencies by any sort of temperature effects. The only other alternative is self-absorption. However, we have shown that the observed effects cannot be entirely due to self-absorption and we are forced to conclude that we must consider together both self-absorption and the b_n's with $\frac{\partial \ln b_n}{\partial h} > 0$ in order to obtain a satisfactory interpretation of the data.

3. Combined Effects of Self-absorption and the b_n's

The only remaining alternative for explaining the changes in β_n with n is to include both the b_n and self-absorption terms in equations (61) and

(79). The χ_m terms are small compared to the effects observed so we will neglect these terms. If we include the absorption terms, we can write (61) as

$$\frac{\partial b_m}{\partial h} + \gamma_m(h) = 2.19 \times 10^{-8} - \beta_m . \tag{83}$$

Also, we can write (79) as

$$\frac{\partial b_m}{\partial h} + \frac{\partial b_m}{\partial n}\frac{dn}{dh} + \gamma_m(h) + \frac{\partial h}{\partial n}\cdot\frac{dn}{dh} = 2.19 \times 10^{-8} - \sigma . \tag{84}$$

Combining (83) and (84), we get

$$\frac{\partial b_m}{\partial n} + \frac{\partial h}{\partial n}\cdot = (\beta_m - \sigma)\frac{dn}{dh} . \tag{85}$$

For the intensity of H_γ at 3000 km $\sigma = 1.88 \times 10^{-8} cm^{-1}$ and for $n \geq 19$ the right side of (85) is negative. The value of σ depends upon the β_n. However, the true β_n must be equal to or greater than the observed β_n. Therefore, the value of σ represents an upper limit and the right side of (85) will actually become negative for some $n \leq 19$. The absorption term on the left of (85) is always positive. Hence, we must have all of the $\frac{\partial b_m}{\partial n} < 0$ at the height appropriate to each n for $n \geq 19$. For $n = 31$, this gives $\frac{\partial b_{31}}{\partial n} < 0$ at 700 km. Since the b_n's must diverge from 1 as n decreases, we must have all b_n's > 1 at 700 km.

The right side of (85) becomes positive for $n < 19$, but since $a_{n,2}$ varies as $1/n^3$ we expect the absorption term to increase in importance as n decreases. However, the rate of increase is not as fast as $1/n^3$ in this case because as n decreases we go to greater heights which decreases the absorption term. In order to have self-absorption more important in H_{10} than in H_{20} we must have

$$\frac{1}{10^3}\, e^{-3\times10^{4}\beta_2} > \frac{1}{20^2}\, e^{-1.5\times10^{5}\beta_2} \tag{86}$$

or

$$\beta_2 < 1.4\times10^{-5}\ \text{cm}^{-1}. \tag{87}$$

This will be the case if

$$-\chi_n \frac{\partial \ln T_e}{\partial h} + \frac{\partial \ln b_2}{\partial h} > 0.8\times10^{-5}. \tag{88}$$

In view of the fact that $\frac{\partial \ln b_n}{\partial h}$ is significant for high order lines and increasing as n decreases, and since we must have relatively high T_e in order to have $b_n > 1$, the inequality in (88) is not unreasonable.

These arguments show conclusively that $b_n > 1$ above 700 km and that they increase with height. We should expect, then, that the observed Balmer decrements would exceed the thermodynamic equilibrium decrements well below the level where self-absorption becomes negligible. Thus we see from Table 8 that the intensities of the lower order lines are reduced by self-absorption up to at least 3000 km. The value of β_2 which we obtained in section 1 was based on the assumption that self-absorption in H_β became negligible at 2000 km. If we had allowed the absorption to persist to higher levels as we should have done, the value of β_2 would have been much less.

If we use the approximation expressed by equation (63) and ignore the small change in $(1 + \frac{\beta_2}{\beta_n})^{-1}$ with n, we see from (64) that

$$\frac{n}{3}\frac{\partial \ln Abs.}{\partial n} = \frac{1}{\beta_2}\frac{\partial \ln Abs.}{\partial h}, \tag{89}$$

and, therefore,

$$\frac{\partial h_m}{\partial n}\frac{\Delta b_m}{\Delta n} = \frac{3}{n\beta_m}\gamma_m(h). \tag{90}$$

Hence, (85) can be written

$$\frac{\partial h_m}{\partial n}\frac{b_m}{\Delta n} + \frac{3\gamma_m(h)}{n\beta_m} = (\beta_m - \sigma)\frac{\partial h}{\partial n}. \tag{91}$$

Since $\frac{\partial h_m}{\partial n}\frac{b_m}{\Delta n} < 0$, we have

$$\gamma_m(h) > \frac{n\beta_m}{3}(\beta_m - \sigma)\frac{\partial h}{\partial n}. \tag{92}$$

At 2000 km and n = 9 $\beta_9 - \sigma \sim -0.68 \times 10^{-8}\,cm^{-1}$ and $\frac{dh}{dn} = -0.17 \times 10^{8}$ cm. Therefore,

$$\frac{\gamma_9}{\beta_2} > 0.35 \tag{93}$$

at 2000 km. From equation (65) with $\beta = 1$, we get

$$N_2\,\alpha_{9,2} > 2.5,$$

and with $\beta = 0$ we get

$$N_2\,\alpha_{7,2} > 1.2.$$

Since $\beta_2 > \sigma$, we can safely say that

$$N_2\,\alpha_{7,2} > 1.2 \tag{94}$$

at 2000 km.

The $\gamma_m(h)$ term in (83) decreases as h and n increase, whereas the $\frac{\partial h_m}{\partial h}\frac{b_m}{\Delta h}$ must increase with height in order to satisfy (83) and it must decrease with n more slowly than $\frac{1}{n^3}$ otherwise both terms on the left of (83) would be negligible for $n \geq 20$. Apparently, then, the $\frac{\partial h_m}{\partial h}\frac{b_m}{\Delta h}$ term in

(83) predominates in all cases except where both n and h are relatively low.

From a physical standpoint, we can now see what is happening to the emission gradients. The self-absorption term in (83) approaches zero asymptotically as both h and n increase. On the other hand, the $\frac{\partial \ln_{n,h}}{\partial \lambda}$ term is approaching asymptotically to a value greater than zero as h increases and the asymptotic value approaches zero as n increases. For n and h such that both terms are reasonably close to their asymptote, their sum is nearly constant. For a lower n and h, the self-absorption term dominates. Hence, the $\frac{\partial \ln_{n,h}}{\partial \lambda}$ term must change more slowly with n and h than the self-absorption term does. However, if for a given n the two terms are approaching their asymptotes at approximately the same rate, their sum will not depart noticeably from a constant until both terms are considerably removed from their asymptotes. As a further illustration of this we can estimate the rate of change of absorption with height and then estimate the changes in the apparent emission gradients.

β_2 is of the order of 1×10^{-8}. Hence, in 1000 km $N_2 a_{n,2}$ changes by a factor e^{-1}. When log Abs. has reached a value of -0.1 the value of $N_2 a_{n,2}$ is small, and log Abs $\approx A_2 \left[1 - \frac{N_2 a_{n,2}}{(1+\beta) \lambda \ln_e} \right]$. At a height 1000 km above the point where log Abs. = -0.1 we have log Abs. = -0.04. A difference in log E_n of 0.06 might well be masked by the random error in the data, and even if it isn't it would not change the gradients appreciably. If, in addition, we have the $\frac{\partial \ln_{n,h}}{\partial \lambda}$ term in (83) partly compensating for the change in the absorption term, we will not detect any change in the emission gradients until /log Abs./ > 0.10. Therefore, we should not be surprised to find that the intensities of the lines are reduced by self-absorption even though we can approximate the log E_n vs. height curves with straight line.

VII. ACKNOWLEDGMENTS

The entire eclipse program of the High Altitude Observatory was supported by the Office of Naval Research and carried out in close cooperation with the Naval Research Laboratory. We wish to express our thanks to Dr. E. O. Hulburt and Dr. John P. Hagen of the Naval Research Laboratory for the many forms of assistance and advice rendered us before, during and after the expedition. We are particularly indebted to them for aid at the eclipse after Dr. Evans' accident and for the close coordination of their radio-noise observations with our optical observations. We also wish to thank Commander W. E. Berg for the excellent manner in which the eclipse expedition was carried out. Our equipment made the difficult trip to the eclipse site in the face of severe complications, on excellent schedule, and without any damage.

In the course of preparing the observing equipment we were forced to turn to many other groups for help. We wish particularly to acknowledge the contributions of the following:

1. Lick Observatory for the use of the Ross lenses;
2. Mt. Wilson Observatory for the loan of a mirror blank for the 24" spherical mirror;
3. Dr. D. H. Mensel for the use of the infrared grating;
4. Dr. David Richardson and the Bausch and Lomb optical company for their excellent and generous work in the preparation of the ultraviolet and visual gratings;
5. Baird Associates for preparation of the optical wedges used in the standardising program;

6. Dr. William F. Swann and the Research Department of Eastman Kodak Company for preparing films for the observations.

In addition we wish to thank members of the shop and research staff of the High Altitude Observatory who contributed so freely of their time and talents when schedule problems made it appear that some of our components might not be ready in time for the expedition.

We are further indebted to Dr. D. H. Menzel for his help and encouragement throughout all phases of the work, and to Dr. R. R. McMath for the use of the microdensitometer at the McMath-Hulbert Observatory.

The author wishes to express his thanks to Dr. W. O. Roberts, Dr. J. W. Evans, Mr. R. H. Lee, and Mr. R. H. Cooper for their support in this work and their many helpful suggestions regarding the reduction procedures; to Mrs. Kathryn M. Virnelson and Mrs. Tursa B. Pflug for help in preparation of the manuscript of this thesis; to Dr. D. K. Billings for his help in solving the complicated photometric problems that faced us; and especially to Dr. R. N. Thomas for his unstinting encouragement and help in all phases of the work.

VIII. APPENDIX

Photometric Data

Table 1.
Optical Constants of Standard Lamp and Collimator and Spectral Attenuation.

λ			λ3500	λ3600	λ3700	λ3800	λ3900
ρ			0.76	0.77	0.78	0.79	0.80
τ $\chi =$		2	0.53	0.51	0.47	0.45	0.43
		4	0.37	0.35	0.31	0.30	0.28
		6	0.21	0.20	0.18	0.17	0.16
		8	0.13	0.11	0.10	0.096	0.089
		10	0.076	0.065	0.063	0.055	0.051
		12	0.046	0.039	0.038	0.033	0.029
		14	0.028	0.024	0.022	0.020	0.018
		16	0.018	0.015	0.013	0.012	0.011
I = 55 amps T = 2567°K	ϵ Jx10^{-9}		0.482 26.3	0.480 35.5	0.478 47.9	0.476 61.7	0.474 77.6
I = 35 amps T = 2428°K	ϵ Jx10^{-9}		0.484 10.7	0.482 14.8	0.480 20.4	0.478 26.3	0.476 33.9
I = 30 amps T = 2281°K	ϵ Jx10^{-9}		0.486 3.55	0.484 5.15	0.482 7.24	0.480 9.78	0.478 12.9
β_λ			0.94*	0.74*	0.64	0.55	0.47

* extrapolated.

Table 2

Standard Exposures Set A

	λ3500		λ3600		λ3700		λ3800		λ3900	
	$\log \frac{dEc}{d\lambda}$	d	$\log \frac{dEc}{d\lambda}$	d	$\log \frac{dEc}{d\lambda}$	d	$\log \frac{dEc}{d\lambda}$	d	$\log \frac{dEc}{d\lambda}$	d
2	13.26	1.99	13.36	2.36	13.43	2.40	13.46	2.47	13.53	2.50
4	13.11	1.80	13.19	2.07	13.25	2.27	13.31	2.38	13.36	2.44
6	12.87	1.46	12.96	1.81	13.01	2.06	13.07	2.23	13.11	2.34
8	12.64	1.10	12.70	1.36	12.77	1.70	12.82	1.92	12.86	2.10
10	12.42	0.82	12.46	1.03	12.56	1.30	12.59	1.53	12.62	1.80
12	12.20	0.54	12.23	0.71	12.34	0.96	12.36	1.16	12.38	1.37
14	11.99	0.33	12.03	0.45	12.10	0.64	12.14	0.81	12.16	0.94
16	11.79	0.21	11.83	0.27	11.88	0.37	11.92	0.48	11.94	0.60
2'	12.47	0.89	12.57	1.20	12.68	1.55	12.77	1.85	12.86	2.10
4'	12.30	0.69	12.40	0.98	12.50	1.24	12.59	1.54	12.67	1.90
6'	12.06	0.46	12.16	0.70	12.26	0.92	12.36	1.17	12.43	1.47
8'	11.81	0.24	11.91	0.40	12.01	0.54	12.10	0.75	12.18	0.97
10'	11.61	0.17	11.69	0.28	11.78	0.39	11.87	0.43	11.94	0.62
12'	11.41	0.15	11.46	0.16	11.56	0.18	11.64	0.23	11.70	0.30
14'	11.20	0.14	11.26	0.14	11.36	0.15	11.42	0.16	11.48	0.17
16'	11.00	0.14	11.06	0.14	11.13	0.14	11.20	0.14	11.26	0.14
Res.	0.07		0.07		0.07		0.06		0.10	

Table 3

Standard Exposures Set B

	λ3500		λ3600		λ3700		λ3800		λ3900	
	$\log \frac{dE_\lambda}{d\lambda}$	d	$\log \frac{dE_\lambda}{d\lambda}$	d	$\log \frac{dE_\lambda}{d\lambda}$	d	$\log \frac{dE_\lambda}{d\lambda}$	d	$\log \frac{dE_\lambda}{d\lambda}$	d
2	13.19	1.84	13.29	2.09	13.37	2.25	13.44	2.35	13.48	2.39
4	13.04	1.64	13.13	1.98	13.19	2.14	13.26	2.26	13.30	2.34
6	12.90	1.38	12.99	1.70	12.95	1.93	15.08	2.12	15.06	2.24
8	12.57	1.04	12.64	1.30	12.71	1.56	12.77	1.80	12.81	2.00
10	12.35	0.74	12.40	1.02	12.50	1.27	12.54	1.40	12.57	1.70
12	12.13	0.48	12.17	0.72	12.28	0.90	12.31	1.04	12.35	1.28
14	11.92	0.30	11.97	0.44	12.04	0.58	12.09	0.68	12.11	0.87
16	11.78	0.20	11.77	0.26	11.82	0.32	11.87	0.40	11.89	0.55
2'	12.47	0.86	12.57	1.12	12.67	1.45	12.75	1.75	12.80	1.98
4'	12.30	0.71	12.40	0.95	12.49	1.22	12.57	1.44	12.63	1.76
6'	12.06	0.48	12.16	0.67	12.26	0.92	12.33	1.11	12.38	1.39
8'	11.81	0.27	11.91	0.37	12.00	0.56	12.06	0.75	12.13	0.94
10'	11.61	0.18	11.69	0.25	11.77	0.31	11.85	0.42	11.89	0.60
12'	11.41	0.16	11.46	0.17	11.55	0.20	11.62	0.25	11.65	0.31
14'	11.20	0.16	11.26	0.16	11.34	0.17	11.40	0.17	11.43	0.19
16'	11.00	0.16	11.06	0.16	11.12	0.16	11.18	0.16	11.21	0.17
Res.	0.14		0.15		0.12		0.11		0.10	

Table 4

Data for Characteristic Curve for Visible Spectrograms at λ4900.

Wedge steps		3	4	5	6	7	8	9	10
Specular density (green)		0.64	0.87	1.22	1.58	1.84	2.12	2.48	2.86
Diffuse densities in wedge image in spectrogram number:	10	0.72	0.56	0.41	0.35	0.32	0.31	0.30	0.29
	13	0.71	0.55	0.40	0.34	0.31	0.31	0.30	0.29
	20	1.22	1.01	0.79	0.64	0.56	0.53	0.51	0.50
	21	1.25	1.06	0.81	0.66	0.58	0.54	0.51	0.50
	22	1.90	1.65	1.30	1.08	0.94	0.84	—	—
log 100 (10^{-D} + 0.036)		1.42	1.23	0.98	0.88	0.71	0.64	0.59	0.57

Table 5

Log_{10} of Relative Intensities in Coronal Continuum at λ4900.

Spec. Number	Exposure time	Height above limb in mm. 0	½	1	1½	2	2½	3	3½	4
10	0.3	1	0.73	0.55	0.37	0.24	—	—	—	—
13	0.3	1	0.74	0.54	0.38	0.24	—	—	—	—
18	0.6	1	0.73	0.55	0.42	0.28	0.17	0.09	-0.01	-0.04
19	0.9	1	0.75	0.58	0.43	0.29	0.20	0.11	0.04	-0.01
20	0.9	1	0.74	0.56	0.40	0.31	0.18	0.12	0.05	-0.01
21	0.9	1	0.75	0.57	0.46	0.31	0.24	0.16	0.08	0.03
22	2.9	1	0.75	0.53	0.35	0.23	0.13	0.07	0.01	-0.02
Average		1	0.74	0.55	0.40	0.27	0.18	0.12	0.03	-0.01
Smoothed Average		1	0.74	0.55	0.40	0.26	0.18	0.10	0.03	-0.03

Table 6

Data for Ultraviolet Characteristic Curves from Coronal Continuum.

Height above limb in mm.		0	½	1	1½	2	2½	3	3½	4
Densities	λ3700	1.18	0.80	0.67	0.53	0.45	0.39	0.35	0.34	0.32
on spectrogram	λ3500	0.77	0.55	0.43	0.34	0.32	0.29	0.27	0.26	0.25
number 16.	λ3450	0.67	0.48	0.38	0.33	0.30	0.28	0.27	0.25	0.25
Densities	λ3900	—	1.58	1.28	1.00	0.83	0.71	0.60	0.54	0.51
on spectrogram	λ3800	1.94	1.48	1.14	0.92	0.78	0.65	0.58	0.51	0.48
number 17.	λ3700	1.76	1.34	1.06	0.84	0.70	0.62	0.52	0.47	0.44
	λ3600	1.54	1.16	0.94	0.75	0.62	0.54	0.40	0.38	0.36
	λ3500	1.28	1.00	0.79	0.65	0.54	0.45	0.40	—	—
	λ3450	1.05	0.85	0.68	0.58	0.43	0.37	0.33	0.30	0.29
Densities	λ3900	—	2.04	1.77	1.54	1.34	1.16	1.03	0.94	0.87
on spectrogram	λ3800	2.39	1.81	1.65	1.42	1.23	1.06	0.96	0.86	0.80
number 18.	λ3700	2.14	1.77	1.50	1.27	1.12	0.97	0.86	—	0.72
	λ3600	1.93	1.60	1.29	1.10	0.97	0.86	0.78	0.69	—
	λ3500	1.79	1.38	1.13	0.96	0.82	0.72	0.64	0.58	0.52
Densities	λ3900	2.55	2.40	2.26	2.15	2.02	1.89	—	—	—
on spectrogram	λ3800	2.48	2.34	2.17	2.03	1.90	1.78	—	—	—
number 20.	λ3700	2.45	2.25	2.09	1.92	1.78	1.68	—	—	—
	λ3600	2.36	2.22	2.04	1.82	1.66	1.46	1.38	1.28	1.16

Table 7

Data for High Density End of λ5700 Characteristic curve.

H_n	Spec. No. 4		Spec. No. 9	
	Log E	d	Log E	d
H_{12}	2.00	2.96	1.87	2.96
H_{13}	1.96	2.96	1.80	2.96
H_{14}	1.89	2.96	1.71	2.90
H_{15}	1.80	2.96	1.63	2.86
H_{16}	1.70	2.91	1.58	2.84
H_{17}	1.60	2.87	---	2.76
H_{18}	1.52	2.87	1.39	2.82
H_{19}	1.48	2.87	1.37	2.80
H_{20}	1.43	2.85	1.28	2.79
H_{21}	1.38	2.82	1.25	2.76
H_{22}	1.32	2.79	1.22	2.74
H_{23}	1.27	2.75	1.18	2.80
H_{24}	1.24	2.72	1.06	2.70
H_{25}	1.22	2.76	1.03	2.65
H_{26}	1.14	2.72	1.00	2.62
H_{27}	1.11	2.61	---	---
H_{28}	1.16	2.63	---	---
H_{30}	1.25	2.65	1.05	2.60

Table 9

Corrections for Exposure Times and

Intensity Ratio in Primary and Secondary Images.

Exp. No.	Planned Time	Data Panel Clocks	Log $\frac{E_{0.1}}{E}$	t (sec.) p = 0.91	Log $E_{pri.}/E_{sec.}$ a	b
2	0.3	—	0.15	0.21	—	—
3	0.3	0.25	0.06	0.25	—	—
4	0.3	—	0.14	0.21	—	—
8	0.3	—	0.10	0.24	2.00	—
9	0.3	0.20	0.18	0.20	1.90	—
10	0.3	—	0.04	0.27	2.15	—
11	0.3	0.20	0.16	0.20	2.20	—
12	0.3	—	0.12	0.23	2.30	2.20
13	0.3	0.22	0.15	0.21	2.00	2.00
14	0.3	—	0.06	0.25	2.25	2.20
15	0.3	—	0.16	0.20	2.10	2.20
16	0.3	0.25	0.06	0.25	2.10	2.15
17	0.3	—	0.18	0.20	2.05	2.10
18	0.3	0.23	0.15	0.21	2.00	2.05
19	0.9	—	-0.22	0.53	2.00	2.00
28	0.9	—	-0.48	1.00	—	—
29	2.9	—	-0.90	2.90	—	—

REFERENCES

1. Hagen, J. P., Naval Res. Lab., Report No. 3504, 1949.

2. Cillié, G. G. and Menzel, D. H., Harvard Obs. Circular 410, Oct. 1935.

3. Goldberg, L., Ap. J. 90, 673, 1939.

4. Redman, R. O., M.N. 102, 140, 1942.

5. Giovanelli, R. G., Australian Jour. Sci. Res. A. 1, 360, 1948.

6. Thomas, R. N., Series beginning with Ap. J. 108, 130, 1948 and ending with Ap. J. 115, 550, 1952.

7. Thomas, R. N., Ap. J. 111, 165, 1950.

7a. Thomas, R. N., Ap. J. 112, 337, 1950.

8. Fowler, F. E. and Johnson, D. S., Electronics 24, 118, 1951.

9. Beck, C. J., Lovell, D. J. and Hulburt, E. O., J.O.S.A. 43, 405, 1953.

10. Forsythe, W. E. and Adams, E. Q., J.O.S.A. 35, 108, 1945.

11. Ornstein, L. S., Physica 3, 561, 1936.

12. Forsythe, W. E. and Worthing, A. G., Ap. J. 61, 146, 1925.

13. Allen, C. W., M.N. 106, 137, 1946.

14. Grotrian, W., Zs. f. Ap. 3, 199, 1931.

15. Strong, J. "Procedures in Experimental Physics", Prentice-Hall, 1949.

16. Thackeray, A. D., M.N. 97, 672, 1937.

17. Kiess, C. C. and Humphreys, C. J., National Geo. Soc., Contr. Tech. Papers, Solar Eclipse Series, No. 2., 53, 1942.

18. Harrison, G. R., Lord, R. C., Loofbourow, J. R. "Practical Spectroscopy", Prentice-Hall, 1948; Forsythe, W. E., "Measurement of Radient Energy", McGraw-Hill, 1937.

19. Wildt, R., Ap. J. 105, 36, 1947.

20. Mitchell, S. A., Ap. J. 105, 1, 1947.

21. Thomas, R. N., Ap. J. 109, 480, 1949.

22. Menzel, D. H., M.N. 92, 820, 1932.

23. Zanstra, H., Proc. Koninklijke Nederlandse Akademie van Wetenschappen, 53, No. 6, 1, 1950 (Circ. No. 1. Astronomical Institute University of Amsterdam.)

24. Matsushima, S., Ap. J. 115, 544, 1952.

25. Matsushima, S., Unpublished communication.

26. Mansel, D. H. and Pekeris, C.L., M.N. 96, 77, 1935.

27. Thomas, R. N., Ap. J. 108, 142, 1948.

DISTRIBUTION LIST

Government Distribution

National Military Establishment

Research and Development Board
1712 G Street, N. W.
New War Department Building
Washington 25, D. C. (2 copies)

Department of the Navy

Chief of Naval Research
Office of Naval Research
Washington 25, D. C.
Attn: Geophysics Branch, Code 416 (3 copies)

Director, Naval Research Laboratory
Washington 20, D. C.
Attn: Technical Information Officer (9 copies)

ONR Branch Offices

Commanding Officer
U. S. Navy Office of Naval Research
Branch Office
495 Summer Street,
Boston 10, Massachusetts

Commanding Officer
U.S. Navy Office of Naval Research
Branch Office
Building 3
N.Y. Naval Shipyard
Brooklyn, New York

Commanding Officer
U.S. Navy Office of Naval Research
Branch Office
The John Crerar Library Bldg., 10th Floor
86 E. Randolph Street,
Chicago 1, Illinois

Commanding Officer
U.S. Navy Office of Naval Research
Branch Office
801 Donahue Street,
San Francisco 24, Calif. (2 copies)

Commanding Officer
U.S. Navy Office of Naval Research
Branch Office
1030 East Green Street
Pasadena 1, California

Other

Office of Assistant Naval Attache
for Research
Naval Attache, American Embassy,
Navy No. 100, Fleet Post Office
New York, New York (2 copies)

Director
Naval Research Laboratory
Washington 20, D. C.
Attn: Optics Division

Chief of Bureau of Ordnance
Navy Department
Washington 25, D. C.
Attn: R3b8

Chief of Bureau of Aeronautics
Navy Department
Washington 25, D. C.
Attn: Navigation Br., AE9

Chief of Bureau of Ships
Navy Department
Washington 25, D. C.
Attn: Code 330
Code 910

Commander
U.S. Naval Ordnance Test Station
Inyokern
China Lake, California

Chief of Naval Operations
Chief, Naval Communications
Navy Department
Washington 25, D. C.

Dr. C. T. Elvey, Director
Geophysical Institute
College, Alaska

Department of the Air Force

Commanding Officer
Army Air Forces
Room 5E-926, Pentagon Building
Washington 25, D. C.
Attn: Mr. J. Weichbrod

Commanding Officer
Air Force Cambridge Research Center
230 Albany Street,
Cambridge 39, Massachusetts
Attn: Dr. Marcus O'Day

Commanding Officer
Wright-Patterson Air Force Base
Dayton, Ohio
Attn: MCREXP-1

Department of the Army

War Department
Office, Chief of Ordnance
Washington 25, D. C.
Attn: ORDTR

Office of Chief Signal Officer
Engineering and Technical Service
Pentagon Building, Room 3B-280
Washington 25, D. C.
Attn: Mr. H. Stulman

Department of Commerce

Director
Bureau of Standards
Washington, D. C.

Central Radio Propagation Lab.
National Bureau of Standards
Washington 25, D. C.
Attn: Director
Mr. A. H. Shapley

Non-Government Distribution

Harvard College Observatory
Cambridge 38, Massachusetts
Attn: Dr. D. H. Menzel

University of Michigan
McMath-Hulbert Observatory
Ann Arbor, Michigan
Attn: Dr. L. Goldberg

Carnegie Institution of Washington
Mount Wilson Observatory
813 Santa Barbara Street,
Pasadena, California
Attn: Dr. S. B. Nicholson
Dr. O. R. Wulf